Informes Técnicos Ciemat 1542

Noviembre, 2024

# SATURATION OF BLOCK/PELLETS BARRIERS OF WYOMING BENTONITE

Villar Galicia, M.V.
Iglesias Martínez, R.J.
Gutiérrez Álvarez, C.

GOBIERNO DE ESPAÑA
MINISTERIO DE CIENCIA, INNOVACIÓN Y UNIVERSIDADES
Ciemat
Centro de Investigaciones Energéticas, Medioambientales y Tecnológicas

Publication available in catalog of official publications


ISSN: 2695-8864
NIPO: 152-24-018-9


Edition and Publication:
Editorial CIEMAT
Avda. Complutense, 40 28040-MADRID
e-mail: editorial@ciemat.es
Editorial news

# ACKNOWLEDGEMENTS

The research leading to these results was financed by the Beacon project, which received funding from the Euratom Research and Training Programme 2014–2018 under grant agreement number 745942. The last phase of the postmortem determinations was financed by the ENRESA-CIEMAT agreement 10522 and the final editing of the report was carried out in the framework of the EURAD-2 project (EURATOM grant agreement No 101166718), WP ANCHORS (Hydraulic mechanical chemical evolution of bentonite for barriers optimisation). The data acquisition system and the sensors' connection systems were prepared by Dr. José Miguel Barcala and the selection of sensors was done by Dr. Pedro Luis Martín. The mercury intrusion porosimetry tests were performed at the Petrophysical laboratory of CIEMAT by N. Brea. The XRD measurements were performed at the High-Level Radioactive Waste Unit of CIEMAT by L. Gutiérrez-Nebot. Ana María Melón of the Hydro-Geosciences Unit of CIEMAT performed the geochemical characterization of the raw samples. The microcomputed tomography analyses were performed at the CENIEH facilities (Burgos, Spain). Juan Aroz and Guillermo García-Herrera participated at different phases in the laboratory work.

# TABLE OF CONTENTS

## LIST OF FIGURES

# LIST OF TABLES

# 1 INTRODUCTION

The sealing ability is a key safety function for bentonite-based barriers in all geological nuclear waste repository concepts. Sealing is achieved by the combination of a high swelling potential and a low hydraulic conductivity. The barriers will be installed as blocks, pellets, and/or granules, which may give place to significant initial heterogeneities in the barrier. In fact, some deep geological disposal concepts are considering the installation around the waste canisters of bentonite barriers made up of two components. highly compacted blocks to support the canister and a granular buffer material consisting of bentonite pellets to fill the rest of the disposal gallery (NAGRA 2019). Although the bentonite buffer shows a natural tendency towards homogenisation, long-term observations both in large-scale and in laboratory tests revealed that a degree of heterogeneity may persist in barrier materials even after full saturation (e.g. García-Siñeriz et al. 2015, Villar et al. 2020, Bernachy-Barbe et al. 2020, Bernachy-Barbe 2021). However, if the homogenization is sufficient to reach the targets for the safety functions after saturation, then the barrier can be assumed to have its assigned properties in the safety case (Sellin 2022). Notwithstanding, bentonite barriers need to be conceptualized such that density variations after hydration are minimized or in the range of the expectations. Otherwise, the effect of a heterogeneous barrier needs to be considered (e.g. advection in the barrier) and/or the design and installation of the barrier components needs to be improved.

All these aspects were tackled in the BEACON project, whose aim was to evaluate the consequences of heterogeneities on the performance of bentonite barriers in geological repositories for high-level radioactive waste, and to develop, test and improve models able to predict the mechanical evolution of installed bentonite components. Among the work undertaken in the project, CIEMAT performed a laboratory experimental investigation about the behaviour upon hydration of binary samples, i.e. samples composed of a block and a mixture of pellets (Granular Buffer Material, GBM), whose initial dry densities and structures noticeably differed (Villar et al. 2021). The bentonite materials used were the same as in the in situ test EB (Engineered Barrier), performed at the Mont Terri underground laboratory in Switzerland (ENRESA 2005, García-Siñeriz et al. 2015): blocks of FEBEX bentonite compacted at a dry density of 1.6 g/cm$^3$ with a water content of 14 %, and a combination of different-size irregular pellets of FEBEX bentonite of water content of ~4 % resulting in an initial dry density for the GBM of 1.3 g/cm$^3$.

In contrast, in the investigation reported here, the block and the pellets/powder mixture had the same initial dry density, and Wyoming-type bentonite was used. Furthermore, regular-shaped pellets ($\phi$=7 mm) were used, mixed in a 70/30 mass ratio with bentonite powder. This kind of pellets and their mixtures with powder were thoroughly characterised in Molinero (2018) and later used in hydration tests by e.g. Darder et al. (2022). They were manufactured from the same material (brand name Laviosa-MPC WH2) as those used in the Full-Scale Seal test (FSS) run by the French nuclear waste agency (ANDRA). This large-scale test aimed to simulate in a surface facility a seal for repositories (Bosgiraud & Foin 2016). In the French repository concept (Cigéo, ANDRA 2013), seals are defined as hydraulic components for closure of large diameter (several meters)

underground installations and infrastructure components such as shafts, ramps, drifts and intermediate level waste disposal vaults. Each seal consists of a swelling clay core (SCC) and concrete containment walls. As SCC, mixtures of 32-mm diameter bentonite pellets and powder were tested and used in the FSS test. At a smaller scale, the complementary REM laboratory test reproduced the same seal concept using the same material as in FSS (Conil et al. 2015). In both cases the SCC consisted of alternating layers of pellets ($\phi$=32 mm) and crushed bentonite (powder) in the mass proportions of 70/30 with a final dry density of 1.50 g/cm$^3$.

The behaviour upon hydration of this mixture was analysed at the laboratory scale in Bernachy-Barbe et al. (2020). They observed local stress heterogeneities that did not disappear upon saturation and were explained by the local environment of the measuring element and small residual density variations. They also detected local density variations in the long term, coming from the pellet/powder structure. It is expected that the combined use of a pellets/powder mixture and a compacted block would give place to more heterogeneous density and stress fields, as was demonstrated in the tests by Martikainen et al. (2018, reported in Talandier 2019), where binary samples of MX-80 bentonite were saturated under constant volume. After a systematic study (Villar et al. 2021) of the behaviour upon saturation of binary samples of FEBEX bentonite (which is predominantly divalent), it was the aim of the experiment reported here to shed light on the stress development upon saturation of a two-part sample of Wyoming bentonite (predominantly sodic), with the additional particularity that in this new test the initial dry density of the two parts was similar, and that a different cell was used in which relative humidity and radial pressures at several locations along the sample were measured.

# 2 EXPERIMENTAL SETUP

The test setup consisted of an instrumented stainless steel cylindrical cell, the hydration system and the control and data acquisition systems (Figure 1). These elements are described in the following paragraphs.

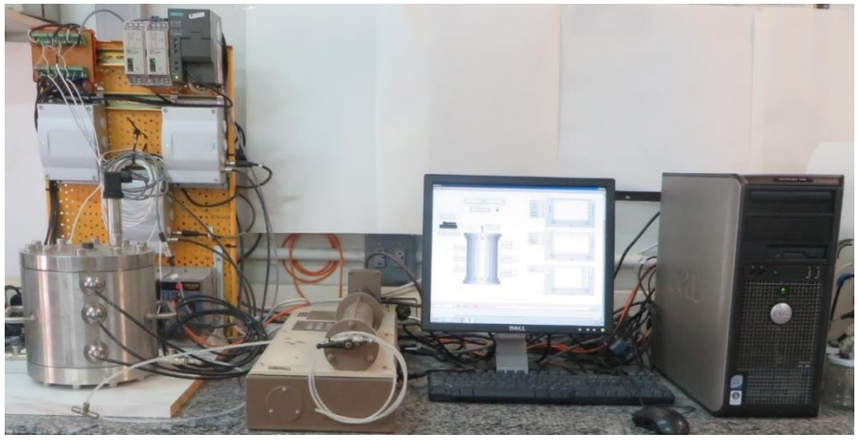

*Figure 1. General setup view*

## 2.1 CELL

A stainless steel cell was used to contain the bentonite. The internal dimensions were 15 cm of diameter and 14.5 cm of height. Figure 2 shows a blueprint of the cell, in which the location of RH/T sensors, pressure sensors and pore pressure sensor is indicated. The sample was hydrated through a porous stone at the bottom.

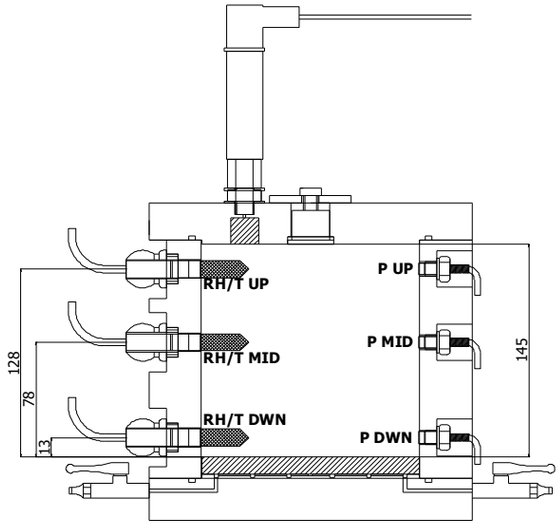


*Figure 2. Longitudinal cross-section of the cell with the sensors installed (RH/T: relative humidity and temperature; P: radial pressure, pore pressure sensor on top)*

## 2.2 SENSORS

### *2.2.1 RH/T TRANSMITTERS*

The cell was instrumented with capacitive-type sensors placed inside the clay at three different levels (13, 78 and 128 mm from the bottom porous stone, Figure 2). The transmitters used were VAISALA HMT337 (Figure 3), which include a humidity sensor (HUMICAP®) that changes its dielectrical characteristics with extremely small variations in humidity (capacitive-type RH sensor). They also include a temperature sensing element (Pt 100). The accuracy of the humidity sensor is ±1 % over the range 0-90 percent RH and ±2 % over the range 90-100 percent RH. The sensors were protected by cylindrical stainless steel filters (HM47280SP, length 41.5 mm, Figure 3).

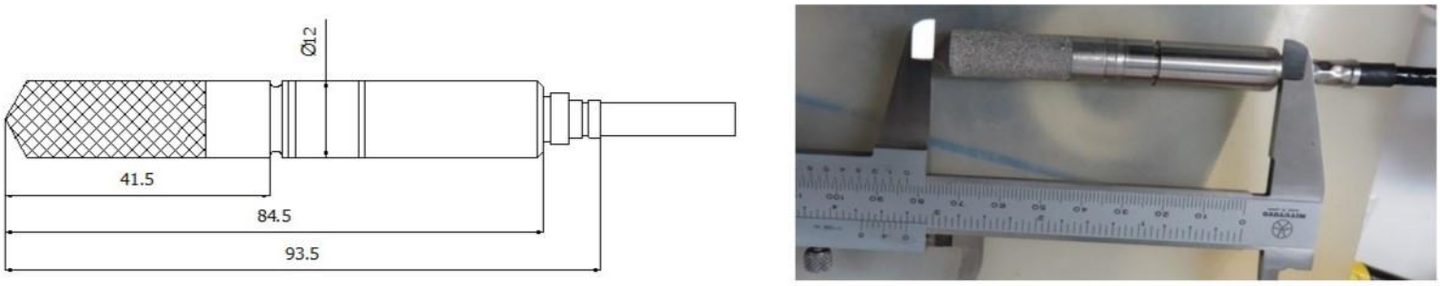


*Figure 3. Vaisala HMT337 relative humidity sensor dimensions*

In order to fit the RH/T sensors in place, cable glands from high-grade stainless steel SKINTOP® INOX were used (Figure 4). These cable glands (SS-316L: gland body and cap nut; silicone: sealing ring and O-ring; M20x1: connecting; IP68-10 bar; temperature range -40°C up to +100°C) allow to modify the installation and fix location problems that could appear (Figure 5).

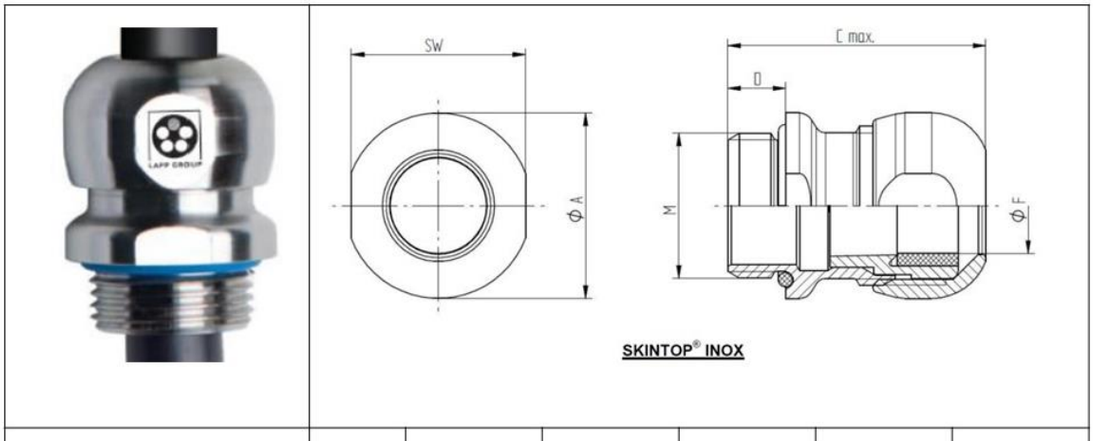


| Dimensions in mm | SW | Ø A | C max. | D | Ø F | O-ring |
|---|---|---|---|---|---|---|
| | 20 | 25.6 | 35.5 | 7 | 7.0-13.0 | 17x2 |

*Figure 4. SKINTOP® INOX M20x1.5 cable gland*

*Figure 5. Insertion of RH/T sensor with cable gland*

### 2.2.2 PRESSURE SENSORS

Radial pressures on the lateral surface of the bentonite cylinder were measured at the same distances from the bottom plate as those for the RH/T transmitters (i.e. 13, 78 and 128 mm, Figure 2). The pressure sensors used were XPM10. Their characteristics are shown in Table 1 and their cross-section and dimensions are shown in Figure 6. These sensors are designed to measure static and dynamic pressure under a wide variety of conditions and are suitable for corrosive liquids and gases in harsh environments. They are made of stainless steel SS316L and their range is 0-100 bar with amplified outputs, with an error of 0.5 bar.

| SENSOR | XPM10-A2-100BS-/ET1 |
|---|---|
| Power supply | ±12 to ±18 Vdc |
| Sensitivity "FSO" | 5 V ±0.2 V |
| Zero Offset | 0 V ±0.2 V |
| Non-Linearity | ±0.25%FS |
| Hysteresis | ±0.25%FS |
| Repeatability | ±0.2%FS |
| Operating Temperature (OTR) | -40 to 80°C |
| Compensated Temperature (CTR) | -20 to 100°C |

*Table 1. Characteristics of the pressure sensors*

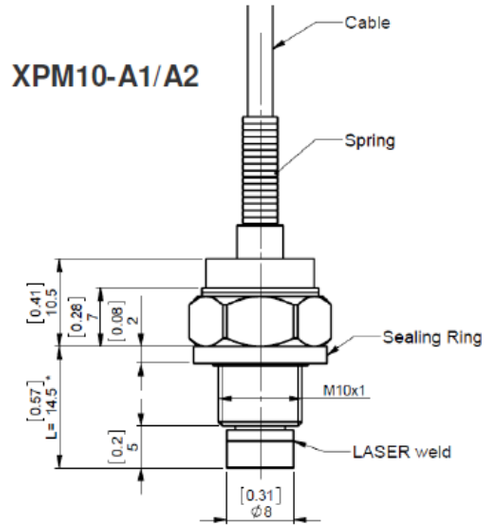


*Figure 6. Blueprint of the total pressure sensors*

### *2.2.3 PORE PRESSURE*

The pore pressure was measured on top of the cell (Figure 2) with a PMP 4070 Druck Amplified Output Pressure Transducer. Its operating absolute pressure range was 700 mbar up to 7 bar. The sensors characteristics are shown in Table 2 and its cross-section and dimensions in Figure 7.

| SENSOR | PMP 4070 |
|---|---|
| Power supply | ±10 Vdc |
| Accuracy | ±0.08% FS BSL maximum |
| Zero Offset | Typical: ±1.5 mV<br>Maximum: ±3.0 mV |
| Stability | ±0.1% FS |
| Operating Temperature Range | -20 to 80°C |
| Temperature effects | ±0.3%FS TEB over 0 to 50°C<br>±1.0%FS TEB over -20 to 80°C |

*Table 2. Characteristics of the pore pressure sensor*


*Figure 7. PMP 4070 Druck pore pressure sensor dimensions*

## 2.3 HYDRATION SYSTEM

The hydration system consisted of a GDS volume/pressure controller (Figure 8) connected to a control PC. Hydration took place with deionised water injected at a constant pressure of 0.014 MPa.


*Figure 8. GDS volume/pressure controller*

## 2.4 DATA ACQUISITION AND CONTROL SYSTEM

The data acquisition and control system was designed as a modular system (Figure 9). Data acquisition of the instrumentation signal was done with a MX100 Yokogawa, which received data from three types of sensors: relative humidity and temperature (RH/T), total pressure sensors and pore pressure sensor. This equipment was connected to a PC by an Ethernet port that allowed to control and display the measurements of the sensors.

The GDS pressure/volume controller was connected directly to the PC.

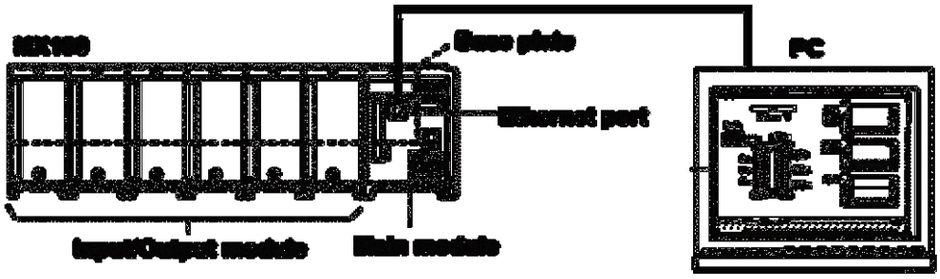


*Figure 9. Data acquisition system*

The MX100 consists of a main module, several input/output modules for connecting signals and a motherboard where all modules are connected. The main module has a connector for power supply (220 Vac), power switch, an Ethernet port, a slot for CF cards and a 7-segment LED display, among other elements. It contains the power supply for all equipment and is responsible for controlling all input/output modules connected to the motherboard. It also manages communications with a computer or other devices via the Ethernet port and saves on the CF card data acquired when communications are disconnected. A motherboard that can accommodate up to four input/output modules in addition to the main module was used. A single type of input/output module was used: the MX110-UNV-M10 (Medium-Speed Universal Input Module). This module has 10 input channels that support signals in DC voltage, TC, 3-wire RTD and digital. Its minimum measuring period is 100 ms. All the signals coming from a cell (3 RH/T sensors, 3 total pressure sensors, 1 pore pressure sensor) can be grouped in a single input module.

The last component of the acquisition system is a PC in charge of data acquisition. LabVIEW was used to develop the data acquisition application (Figure 10), which allowed the configuration of different parameters, asked for the data to the different nodes, showed the data on screen and recorded them in a file. This program displayed an interface on the screen with the location of each sensor, with values in real time, as well as a series of graphs showing the evolution of the different parameters over time. Data for relative humidity, temperature, lateral pressure, pore pressure, and volume and pressure of the GDS volume/pressure controller were recorded and shown on the screen. The data collection frequency could be configured as desired.

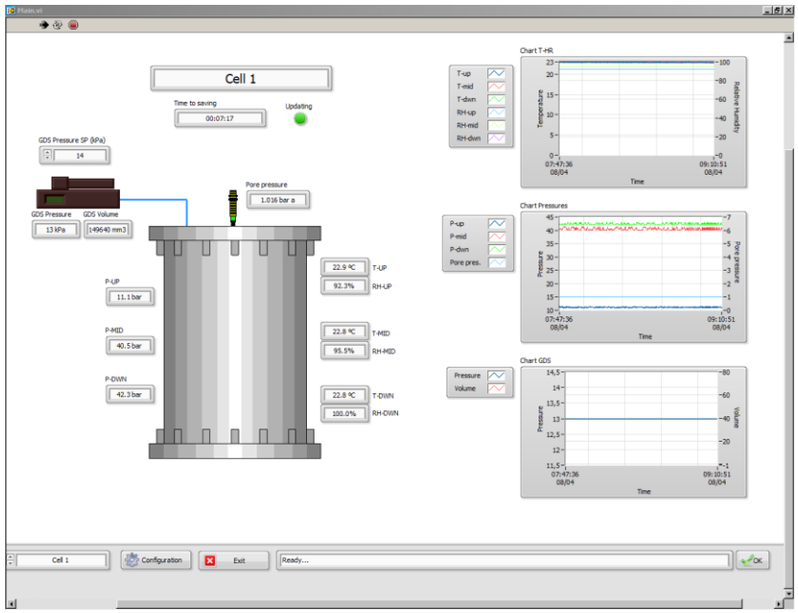


*Figure 10. Interface of program Labview for tests control*

# 3 MATERIALS

The test was performed with an MX-80 bentonite block and a mixture of Wyoming-type bentonite pellets and powder in a mass ratio 70/30, a granular buffer material (GBM, Figure 11). The block was obtained by powder compaction, and the same powder was used in the pellets/powder mixture. The initial water content of the bentonite powder was 8.9 % and of the pellets 6.2 % (Table 3). The pellets had a regular, approximately spherical shape with a diameter of 7 mm and a dry density of 2.0 g/cm$^3$. They were provided by AITEMIN in 2013 (in turn supplied by Laviosa MPC) in the framework of the in situ test NSC, performed at the Bure URL in France. They were manufactured from the material with brand name WH2, but no detailed mineralogical characterisation of the pellets was provided by the suppliers nor performed at CIEMAT. The manufacturer of the pellets (Laviosa MPC) provided a mineralogical composition of 80 % montmorillonite, 8 % anorthite, 4 % quartz, 4 % muscovite and 2 % pyrite (Molinero-Guerra 2018). Bosgiraud & Foin 2016 characterised the 7-mm diameter pellets, and found for them a dry density of 2.00 g/cm$^3$, a water content of 4.9 % and a particle density of 2.78 g/cm$^3$ for the material from which they were produced. The particle density obtained at CIEMAT for the pellets was 2.75 g/cm$^3$.

| VARIABLE | PELLETS | POWDER |
|---|---|---|
| Grain size (mm) | 7.0 | 0.14 - 0.75 |
| Average particle volume (cm$^3$) | 0.24 | - |
| Bulk density (g/cm$^3$) | 2.1 | - |
| Dry density (g/cm$^3$) | 2.0 | - |
| Water content (%) | 6.2 | 8.9 |

*Table 3. Characteristics of the MX-80 pellets and powder*

*Figure 11. Appearance of MX-80 bentonite powder (left) and MX-80 pellets (right)*

The MX-80 bentonite is a brand name used by the American Colloid Company for sodium bentonite from Wyoming (USA), milled to millimetre-sized grains. According to studies performed in different batches of this bentonite by different authors, the content of montmorillonite can be between 65 and 90 %, with quartz, plagioclase and K-feldspars (contents between 4 and 15 %), and minor quantities of cristobalite, tridymite, calcite, gypsum, pyrite, illite. The cation exchange capacity is 75-82 meq/100g. $Na^+$ is the main exchangeable cation (50-74 meq/100 g), with also $Ca^{2+}$ (10-30 meq/100 g) and $Mg^{2+}$ (3-8 meq/100g). The main soluble ions are sodium and sulphate.

In the batch used to compact the block and for the powder in the mixture, the smectite content was 92 %, the feldspars content 5 % and the quartz content 1 %, with traces of calcite, gypsum, dolomite, halite and pyrite (Gómez-Espina & Villar 2016). The particle density was 2.78 g/cm$^3$.

A specific geochemical characterisation was performed for the two raw materials used in this test (pellets and powder). The concentration of ions measured in aqueous extracts of solid:liquid ratio 1:8 is shown in Table 4. Table 5 shows the cations extracted using a solution 0.5 M of $CsNO_3$ at pH 8.2 and the CEC of the raw samples. Since the methodology followed for the extraction of exchangeable cations did not involve previous washing of the samples, both exchangeable and soluble cations were actually measured in the extracts prepared. For this reason the values given correspond in fact to “extractable” cations, in the sense that they may include soluble cations in addition to the exchangeable ones. As well, during the preparation of the extracts some species could be dissolved and the cations released could enter the exchangeable complex, substituting for other cations. This could be particularly the case of calcium substituting for sodium. All the values given in these Tables are the average of two measurements.

| REFERENCE | pH | Alkalinity | $Ca^{2+}$ | $Na^+$ | $K^+$ | $Cl^-$ | $SO4^{2-}$ | $HCO^{3-}$ |
|---|---|---|---|---|---|---|---|---|
| Powder | 8.4 | 5.2 | 0.2 | 16.2 | 0.2 | 0.2 | 10.1 | 5.2 |
| Pellets | 8.8 | 6.0 | 0.1 | 13.3 | 0.2 | 0.2 | 6.7 | 6.0 |

*Table 4. Analysis of the 1:8 aqueous extracts of the raw bentonite materials (meq/L)*

| REFERENCE | $Na^+$ | $K^+$ | $Mg^{2+}$ | $Ca^{2+}$ | $Sr^{2+}$ | Σ extract. | CEC |
|---|---|---|---|---|---|---|---|
| Powder | 63 | 1.9 | 6 | 20 | 0.2 | 91 | 77 |
| Pellets | 61 | 2.0 | 5 | 18 | 0.1 | 86 | 71 |

*Table 5. Extractable cations and CEC of the raw bentonite materials (in meq/100 g)*

The swelling pressure of small samples (3.8 or 5.0 cm in diameter, 1.2 cm in height) of MX-80 bentonite powder compacted with its hygroscopic water content was determined at CIEMAT at room temperature using deionised water as saturation fluid in standard oedometers. The swelling pressure ($P_s$, MPa) could be related to the final dry density of the sample ($\rho_d$, g/cm$^3$) through the following equation (Villar 2013):

$$\ln P_s = 5.44\ \rho_d - 6.94 \qquad [1]$$

The hydraulic conductivity ($k_w$, m/s) of samples of powdered MX-80 bentonite (grain size <1 mm), compacted at different dry densities ($\rho_d$, g/cm$^3$) and kept in stainless steel cells which hindered the swelling of the material upon saturation, was measured in a constant head permeameter (Villar 2005). Deionised water was used as permeant. The following exponential relation between dry density ($\rho_d$, g/cm$^3$) and hydraulic conductivity ($k$, m/s) was found:

$$\log k_w = -2.94\ \rho_d - 8.17 \qquad [2]$$

# 4 SAMPLE PREPARATION

The test was performed with the bentonite compacted block in the upper part and the pellets/powder mixture at the bottom part of the cell (Figure 12)

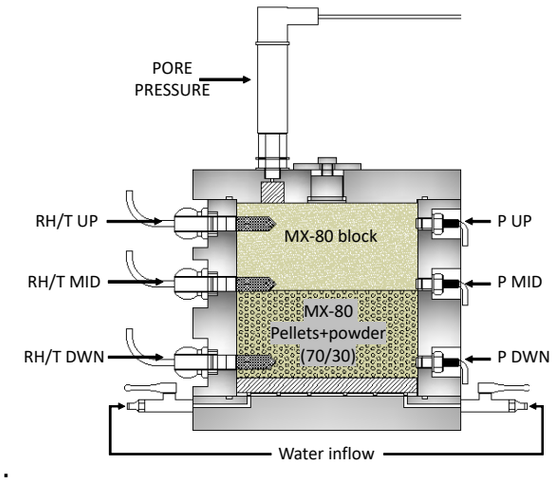


*Figure 12. Cell configuration in test CT31*

The block was compacted at a dry density of 1.50 g/cm$^3$ inside the cell body placed upside down using a uniaxial pressure of 11.4 MPa. Then the other half of the cell was filled with the mixture of pellets and MX-80 powder. This mixture was arranged in 8 layers in such a way that the powder filled the gaps between the pellets. Each layer consisted of a first level with 1/3 of powder (~26 g), a second level with the pellets (~179 g), and a third level with the remaining 2/3 of powder (~52 g) (Figure 13). During the process, light blows were given to the cell to readjust the particles so that the mass necessary to reach the target dry density of 1.50 g/cm$^3$ could fit inside. Once a layer was completed, a light pressure was applied to the mixture surface using a circular plate of the same diameter as the cell, so that to get an even layer surface. A total of 1433 g of pellets (1349 g dry mass) and 629 g of powder (578 g dry mass) were used for the mixture part. The bottom RH/T sensor was inserted as the cell was being filled (Figure 13, middle).

*Figure 13. Preparation of the pellets/powder mixture half of the sample. The middle photo shows the bottom RH/T sensor in place*

The initial characteristics of the material inside the cell, including water content ($w$), dry density ($\rho_d$), degree of saturation ($S_r$) and height ($h$) can be seen in Table 6.

| VARIABLE | $w$ (%) | $h$ (cm) | $\rho_d$ (g/cm$^3$) | $S_r$ (%) | Volume (cm$^3$) | Dry mass (g) |
|---|---|---|---|---|---|---|
| Pellets/Powder mixture | 7.0 | 7.20 | 1.50 | 23 | 1,281.30 | 1,927.20 |
| Block | 8.9 | 7.25 | 1.49 | 29 | 1,286.70 | 1,934.00 |
| Average / (Total) | 8.0 | (14.45) | 1.50 | 26 | (2,578.6) | (3,861.1) |
| After drilling | - | - | - | - | 2,568.00 | 3,845.60 |

*Table 6. Initial characteristics of the materials of test CT31*

After filling and closing the cell, the middle and upper RH/T sensors were installed. To insert them the bentonite was drilled with a bit of the same diameter as the sensor (12 mm). The material expelled during drilling was recovered and weighed (the corrected initial weight and volume are indicated in Table 6). Afterwards, the sensors were quickly inserted (Figure 14). The pore pressure sensor was fixed to the upper lid of the cell. The pressure sensors were screwed to the cell body in contact with the external surface of the bentonite cylinder (Figure 15).

*Figure 14. Placement of the middle and upper RH/T sensors*

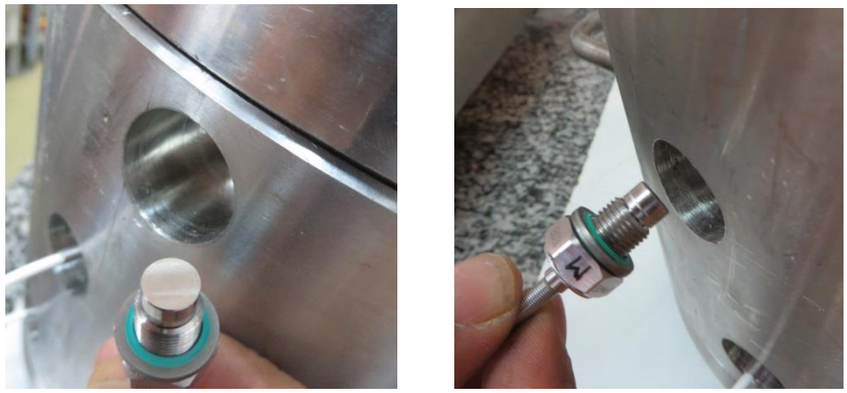

*Figure 15. Placement of pressure sensors*

The data recorded by the sensors once installed and before the start of operation are shown in Figure 16. Hydration started six days after the cell was assembled. During this time the RH inside the block slightly decreased, whereas that of the mixture (bottom) slightly increased. This effect was triggered by the initial difference in water content of both materials (8.9 *vs.* 7.0 %). A shorter stabilisation time would have avoided this initial water transfer. The values measured just before hydration are shown in Figure 17.

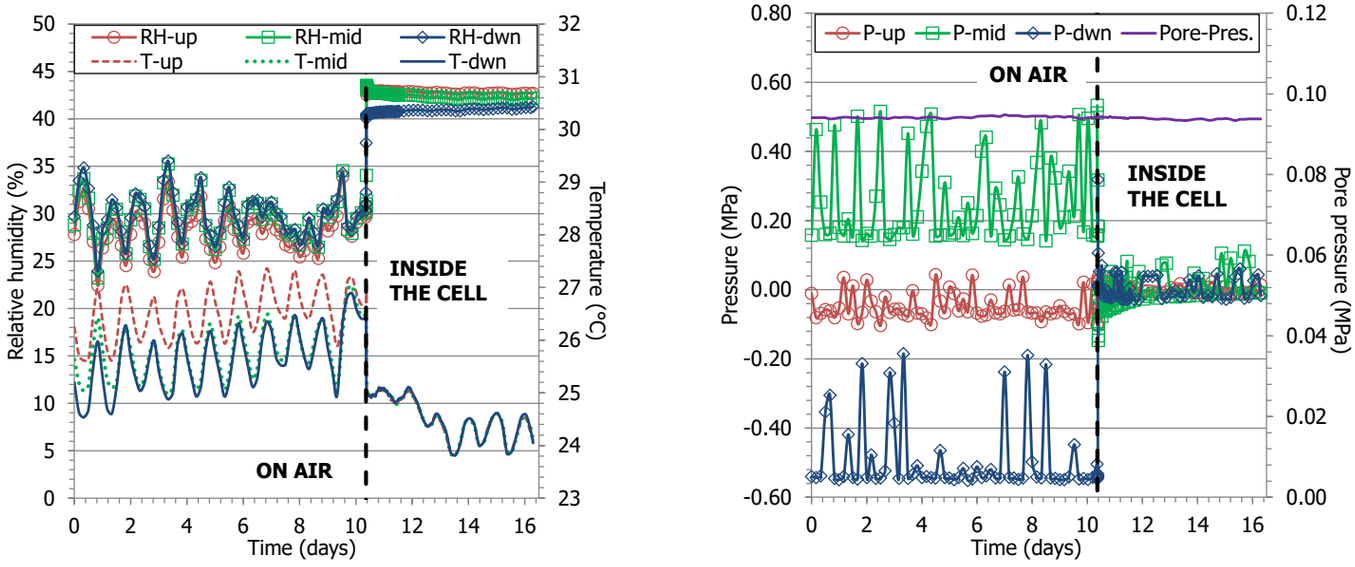


*Figure 16. Recordings of the sensors on air and inside the cell before hydration (a) TH/T and (b) Pressure*

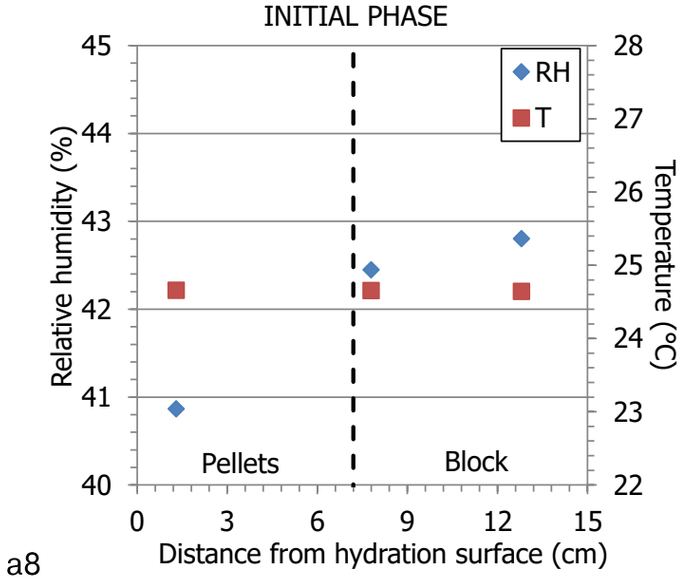


*Figure 17. RH/T inside the cell just before hydration*

# 5 ONLINE RESULTS

Deionised water was injected at a pressure of 0.014 MPa using a GDS volume/pressure controller. The water intake was faster at the beginning because of the volume of water necessary to saturate the porous stone and the high porosity of the mixture. In the first two hours the water intake was so quick that the injection pressure could not reach the target value. It is considered that most of this water filled the hydration ducts inside the bottom lid and the lower porous stone. This value was in fact checked at the end of the test, when the cell was dismantled (see section 6.2), and has been subtracted from the initial water intake as shown in Figure 18. Considering this correction, and after approximately 600 days, the water intake stabilised at a value of ~893 $cm^3$. During this time gas bubbles were occasionally observed in the hydration line, which had to be periodically vented.

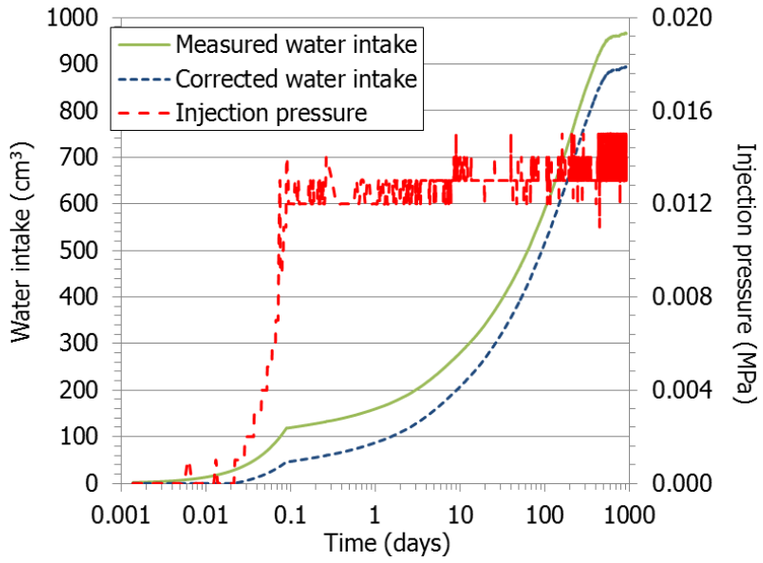


*Figure 18. Measured and corrected water intake and injection pressure in test CT31*

The RH/T sensor at the bottom was quickly flooded because of the high permeability of the low-density mixture (Figure 19). In an attempt to solve the premature loss of information from one of the sensors, it was removed from the cell and dried. Then the sensor was inserted again and its correct performance was checked. Hence, the relative humidity at 13 mm from the hydration surface was 100 % almost from the beginning. The sensors' recordings during the whole test duration are shown in Figure 20. After 2 years of hydration, consistently with the stabilisation of water intake, the RH at all positions inside the bentonite was around 100 %.

The pressure sensors operated correctly since hydration started (Figure 21). The bottom sensor recorded a quick and steady pressure increase. The middle sensor recorded initially a soft decrease, probably reflecting the collapse of the pellets part on saturation. Afterwards the middle sensor recorded a considerable increase in a relatively short period of time (from 0 to 4.3 MPa in 60 days) followed by a soft decrease and a new constant increase. It took longer for the upper sensor to start recording any pressure (~200 days), but then it

continuously increased. After ~700 days of hydration the three radial pressure sensors recorded steady values, with the middle sensor recording the highest one (6.4 MPa) and the bottom sensor the lowest one (4.6 MPa). This reflects the dry density gradient in the bentonite, where the lower part, which was first saturated, could swell more (see section 8.1).

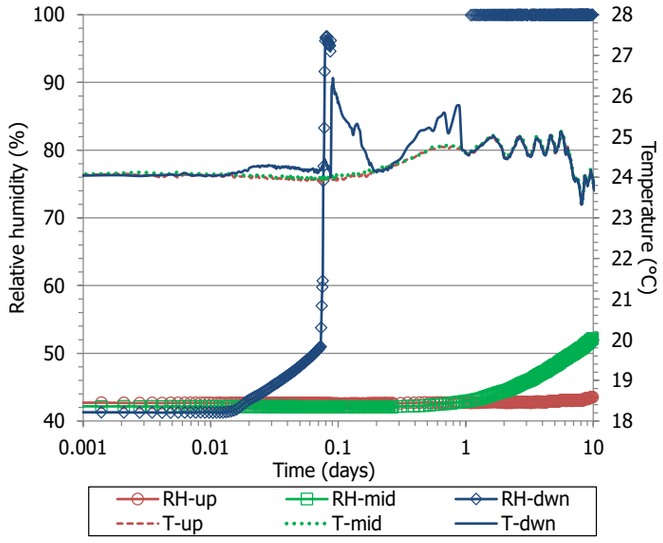


*Figure 19. Relative humidity and temperature evolution at the beginning of hydration*

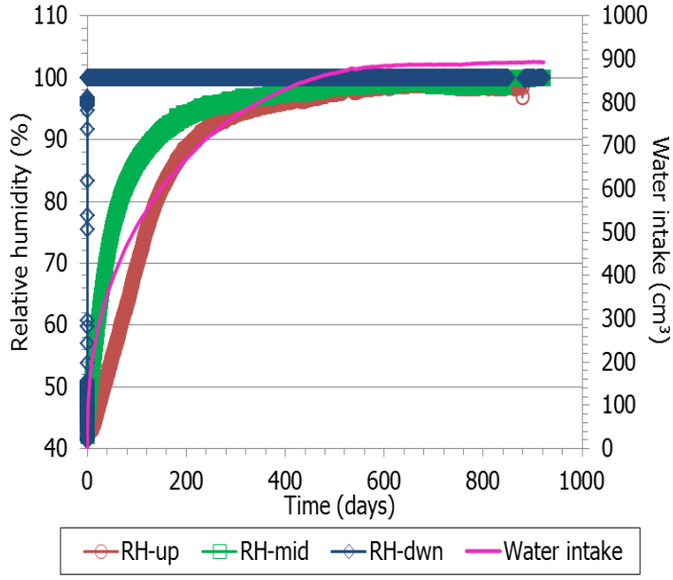


*Figure 20. Relative humidity, temperature and water intake evolution during hydration*

As well, the pore pressure sensor on top of the cell did not record any change until 500 days had elapsed, and afterwards it steeply increased, reaching an equilibrium value of ~180 kPa.

A summary of the values recorded by the sensors during operation is given in Appendix I.

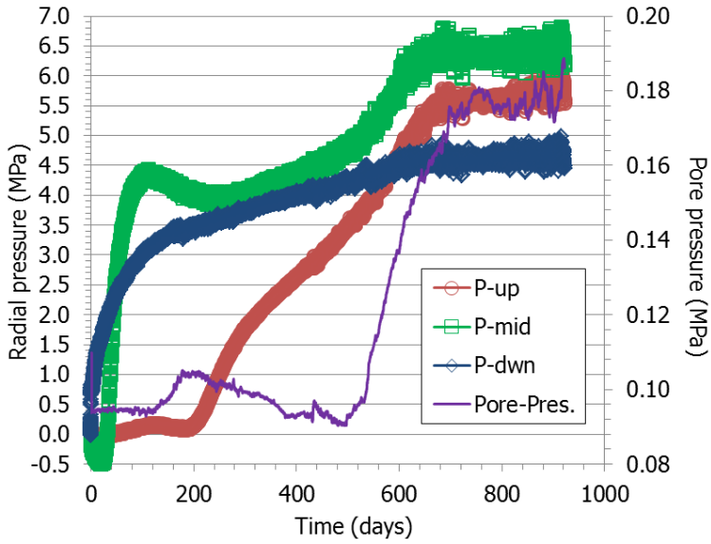


*Figure 21. Radial pressure and pore pressure evolution during the hydration phase*

# 6 CELL DISMANTLING AND SAMPLING

The cell dismantling was accomplished on February 7th 2022, after 922 days of hydration, and comprised two phases. The first one consisted of ending hydration, disconnecting cables and tubes and removing sensors; and the second one consisted of the extraction and sampling of the bentonite column. The whole process was carried out in the same laboratory.

## 6.1 ENDING OF OPERATION

The first dismantling phase followed the steps described below, with indication of the exact time of some of the operations:

1. The data acquisition interval was changed to 1 minute (8:58).
2. The water injection line was closed (8:58).
3. The pore pressure sensor was removed, and the opening closed (9:01, Figure 22)
4. The RH/T sensors were disconnected and extracted. The sensing elements were first extracted (Figure 23), because the stainless steel filters were stuck inside the bentonite and had to be extracted later (see bullet 6 below). The RH/T upper sensor (extracted 9:04-9:10) as well as the middle one (extracted 9:10-9:16) had some water inside. In contrast, the bottom RH/T sensor was dry (extracted 9:16-9:22).
5. The pressure sensors were disconnected and removed with a pipe wrench (Figure 24, left). The upper one (extracted 9:23) showed some adhered clay (Figure 25 , right), whereas the middle one (extracted 9:25) and bottom one (extracted 9:26) were found to be clean. As the sensors were removed, the threaded holes in the cell were plugged with nuts to prevent water loss.
6. The stainless steel filters of the RH/T sensors that had remained inside the bentonite were removed by screwing them in a bespoke piece that was used to pull them out (Figure 25). Upon extraction the voids left were filled with Teflon plugs. None of the sensors showed any rust stains, and all were in good state. However, the bottom RH/T sensor was found to be slightly bent.
7. From 12:42 the time of data acquisition was changed to 1 hour and the sensors were left measuring in the air to check their performance.

*Figure 22. Removing of the pore pressure sensor*

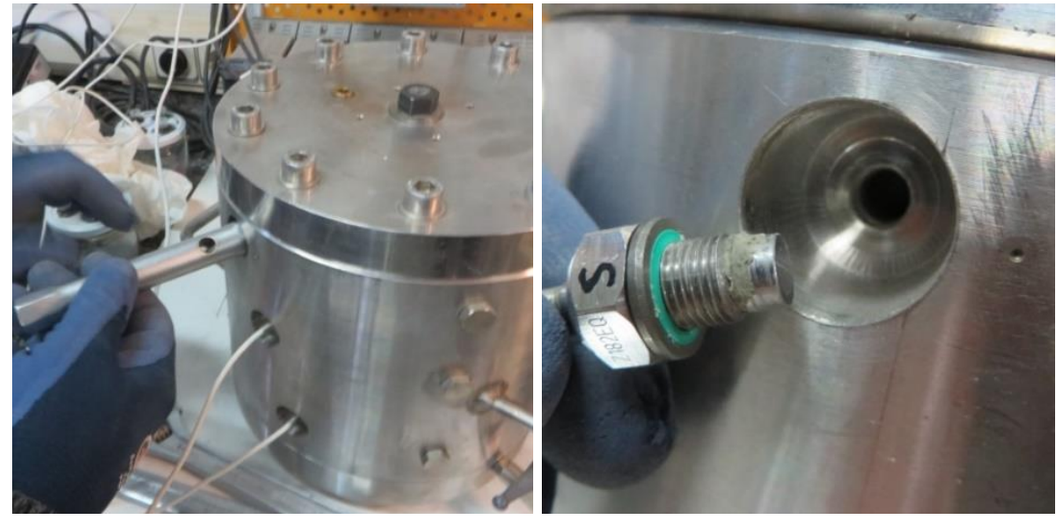

*Figure 24. Removal of pressure sensors and appearance of the upper one*

*Figure 23. Removal of upper (left), middle (middle) and bottom (right) RH/T sensing elements*

*Figure 25. Sintered filters of RH/T sensors. Up (left), Mid (middle) and Dwn (right) slightly bent*

## 6.2 CELL DISASSEMBLING AND BLOCK EXTRACTION

The second dismantling phase proceeded following approximately the steps described below.

1. The cell was weighed before disassembling it (Figure 26).

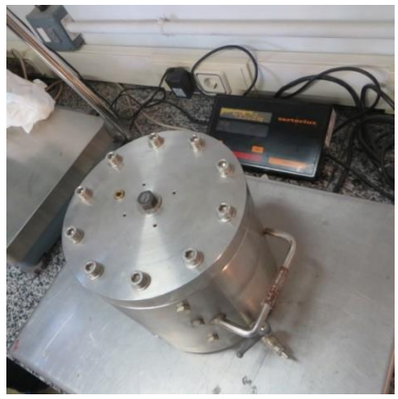

*Figure 26. Weighing of the cell before disassembling*

2. The top cover was removed. Some water droplets were visible on the inside surface. The filter paper that had been initially placed on top of the bentonite kept its initial appearance, and although it was stuck to the clay, it was not uniformly wet (Figure 27, left). The exposed area was then covered with plastic film during subsequent handling to prevent moisture loss.

3. The lower cover was removed. The porous stone through which hydration took place had numerous black spots irregularly distributed over the surface. It was later observed that the filter paper that had initially been placed in that area (between the porous stone and the bentonite) had practically disappeared (Figure 29, left). The black spots on the porous stone could correspond to areas of fungal growth (Figure 27, right).

*Figure 27. Upper (left, filter paper) and bottom (right, porous stone) elements inside the cell*

4. The clay block was extracted from the cell using a steel piston placed on top of the sample to which pressure was applied with a press (Figure 28). No significant pressure had to be applied for the bentonite to come out into the hollow steel cylinder placed below the testing cell. The impact of the sample on the bottom surface was cushioned by a layer of rubber and paper. The sample maintained its cohesiveness and consistency during extraction, handling, section cutting and subsequent sampling.

*Figure 28. Extraction of the sample with a uniaxial press (left), and sample once extracted (right)*

5. The bentonite block was photographed, measured and weighed (Figure 29), as well as all the elements that came out with it (porous stone, filter paper and Teflon plugs) and the clay adhered to the inside of the extraction mould and cell. The block was then protected with plastic film, inside a custom-made plastic pot, to avoid loss of mass during subsequent manipulations and cuttings.


*Figure 29. Final appearance of the bentonite block*

The bentonite block had a homogeneous appearance, it was dark and no pellets or other distinctive elements could be told apart. In fact, the separation between pellets and block was not clear, but it seemed to be at ~7 cm from the bottom surface. Upon extraction the final height of the sample was 14.54 cm, slightly higher than

the initial one (14.45 cm, Table 6). No change in diameter was detected. Hence the dry density of the block once extracted would be 1.49 g/cm$^3$.

The elements of the cell (porous stone, filter papers, top and bottom lids, sensors' filters) were weighed just after disassembling and then again once they were clean and dry, which allowed to compute the water taken by the cell elements, approximately 76 g. Most of it was probably taken at the very beginning of the experiment (the bottom porous stone took 68 g of water), and for this reason this quantity has been subtracted from the initial water intake, as shown in Figure 18.

The final weight of the bentonite was calculated considering all the intermediate weights taken for the different elements during the process described above. The most realistic value obtained was 5020.31 g. According to the theoretical initial and dry weights of the sample (Table 6), this would correspond to a water content of 30.5 % and a degree of saturation of 100 %.

## 6.3 BENTONITE SAMPLING AND ASSESSMENT OF FINAL STATE

The bentonite column was consistent and easy to handle and it could be easily sectioned using a saw. Saw cuts were made to obtain seven slices or horizontal sections (Figure 30, Figure 31), covering the compacted block area (sections 1B-3B), the mixture area (sections 5P-7P), and the contact area between both (section 4BP). In order to obtain an overall (approximate) value of the density of each section, they were weighed and measured with a calliper (Figure 31, middle).

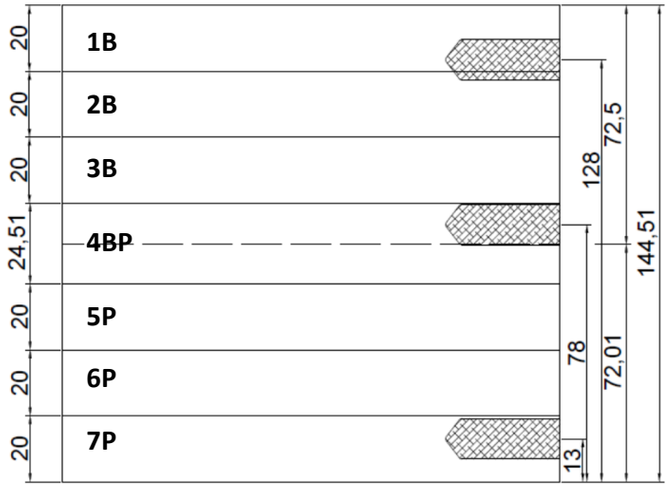


*Figure 30. Subsampling of the bentonite column in horizontal slices (1B to 7P) and indication of the position of the RH/T sensors on the right (dimensions in millimetres, values according to initial measurements)*

Within each section a series of samples were taken to analyse the state of the bentonite in the inner, outer and intermediate areas of the bentonite column. For this purpose, a cross-shaped scheme covering the three areas was followed. Figure 32 gives an example of the subsampling done in section 1B, and the same information is

given in Appendix II for the other sections. For each slice four samples were obtained in the external ring, four in the middle ring and a central sample, i.e. a total of nine samples per slice. Each of these samples was cut into two pieces, one was used for water content and dry density determination (samples ρ) and the other one for water content measurement (samples w). The remaining four quadrants were numbered 1 to 4 and parts of them were used for other types of analyses (MIP, BET, XRD, micro-CT and stereo microscope observation).


*Figure 31. Cutting of a section (left), weighing of the slice obtained (middle), and cutting of subsamples (right)*

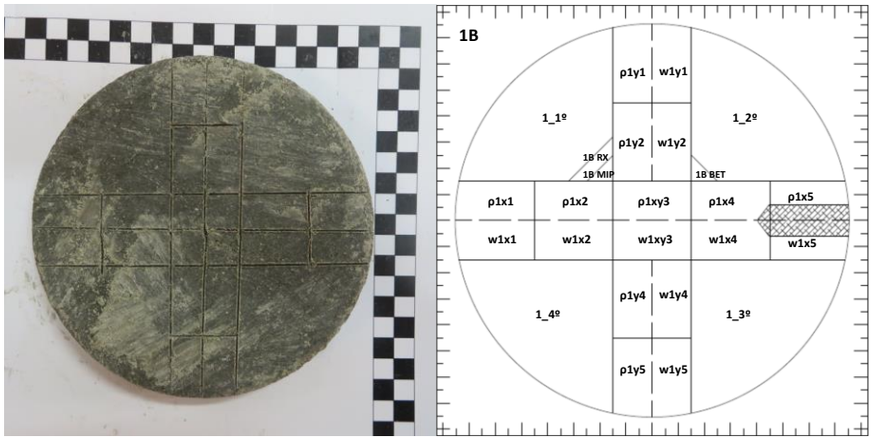


*Figure 32. Appearance of a section before being cut into subsamples (left), and sampling scheme (right) with reference to the type of determination (ρ: dry density, w:water content, RX:XRD, MIP, BET)*

The samples from section 4BP, containing the block/mixture contact, were more carefully inspected. Images of this area are shown in Figure 33. As it was commented above, it was not easy to tell apart mixture from block, although in some slashes the mark left by the knife was different in the block and the mixture parts.

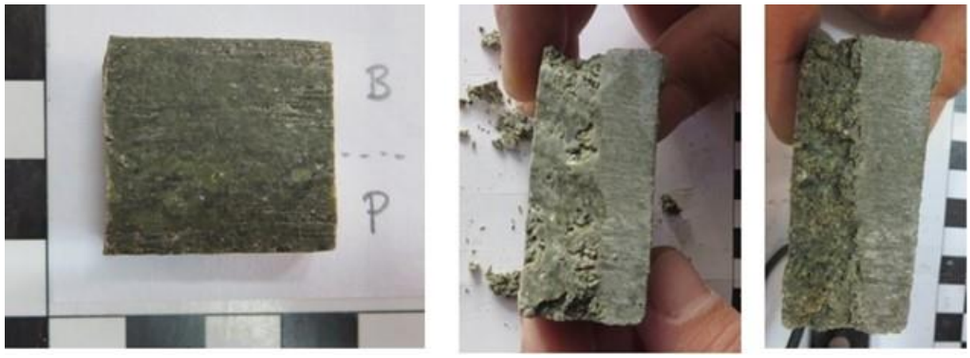


*Figure 33. Appearance of fragments from slice 4BP (pellets/block contact). In the middle and right images the pellets part is on the left*

Some of these samples were dried in the oven and their final appearance is shown in Figure 34. On the left hand side of the Figure, the mould of sensor 2 inside the bentonite block can be observed. Nevertheless, even after drying it was difficult to separate the two parts.

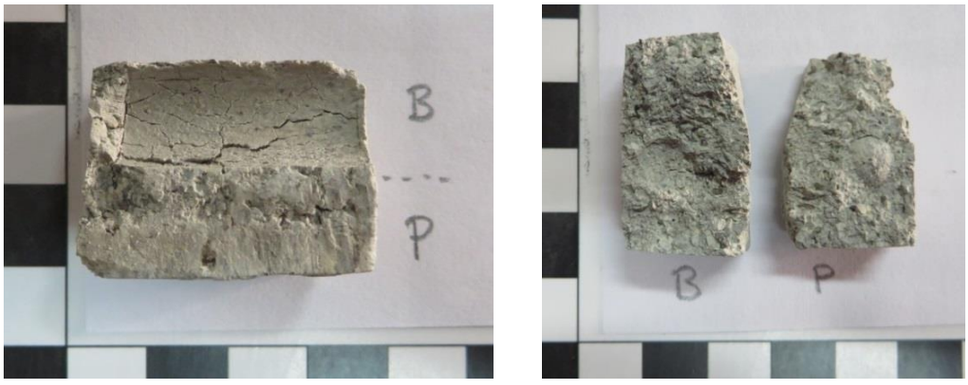


*Figure 34. Appearance after drying of the block/mixture contact. (Left) area where sensor 2 was located. (Right) the shape of a spherical pellet and its mould in the bentonite block can be observed*

# 7 ASSESSMENT OF SENSORS PERFORMANCE

The RH/T and pressure sensors were left measuring in the air after they were extracted from the bentonite and cell (Figure 35). Despite having performed well during the test, the sensor on top of the cell did not resume proper measurement after it was extracted from the cell. The other two sensors recorded in the air similar values of relative humidity and temperature. The sensors and filters were cleaned one day after dismantling, but this did not result in any change in the measurement trends. Figure 36 shows the recordings of the stress and pore pressure sensors. The measurements in the air of the stress sensors were very similar to those recorded before the initiation of the test (Figure 16).

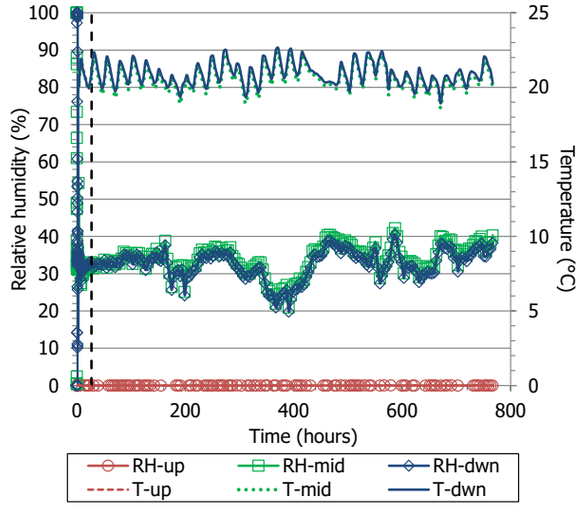


*Figure 35. Recordings of RH/T sensors in the air after dismantling (the vertical dotted line indicate the moment the sensors were cleaned)*

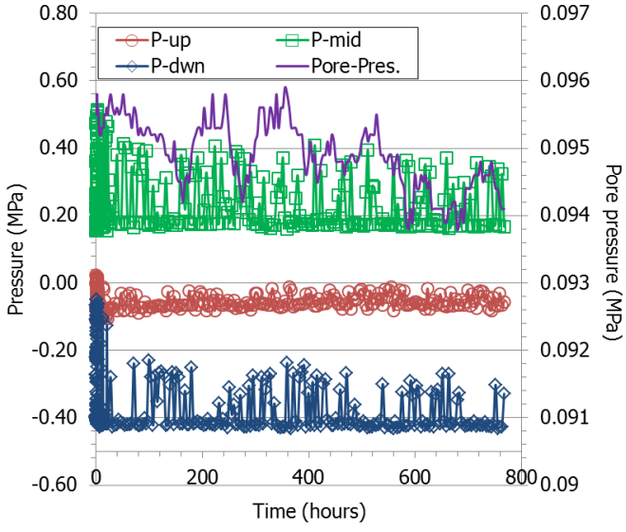


*Figure 36. Recordings of the pressure sensors in the air after dismantling*

# 8 FINAL STATE OF THE BENTONITE

## 8.1 DRY DENSITY AND WATER CONTENT

### *8.1.1 METHODOLOGY*

The gravimetric water content (*w*) is defined as the ratio between the mass of water and the mass of dry solid expressed as a percentage. The mass of water was determined as the difference between the mass of the sample and its mass after oven drying at 110°C for 48 hours (mass of dry solid). The samples used for the water content determination had masses between 8.5 and 19.6 g, with an average of 13.5±2.0 g.

Dry density ($\rho_d$) is defined as the ratio between the mass of the dry sample and the volume occupied by it prior to drying. The volume of the specimens was determined by immersing them in a recipient containing mercury and by weighing the mercury displaced, considering a density of mercury of 13.6 g/cm$^3$. The absolute error of this measurement is in the order of $10^{-2}$ g/cm$^3$. The volume of the samples used for this determination ranged between 5.8 and 13.2 cm$^3$, with an average of 9.5±1.4 cm$^3$. The same samples whose volumes had been determined were used for an additional water content determination (subsamples $\rho$ in Figure 32). However, this value was only used as a cross-check and the water content determined in dedicated samples (just oven dried, subsamples w in Figure 32) was the one used to compute the dry density.

The balance used was an AND GF2000, with a capacity up to 2,100 g and a precision of 0.01 g.

### *8.1.2 RESULTS*

The values obtained are summarised in Table 7 to Table 9, where average values for slice and area (external, middle and internal) are included. The values obtained for each sample are shown in Appendix III. The average water content of the block would be 30.0 %, which is slightly lower than the value reported in 6.2 obtained from the final weight (30.5 %). This is reasonable, since even careful handling of wet samples cannot avoid certain drying during manipulation. The final dry density obtained from thefinal block dimensions is the same as the average obtained from the different measurements.

Figure 37 shows the water content and dry density values obtained along the bentonite column and Figure 38 the degree of saturation computed from them. The water content was higher in the 3 cm closest to the hydration surface, increasing towards it, but was homogeneous in the rest of the column, with values between 29 and 30 %. The water content determined in the external ring of the column, i.e. in the bentonite in contact with the cell wall, was higher than the internal one both at the bottom and on top of the column. Conversely, the dry density on these areas was consistently lower. This could mean that, at least initially, the contact between the cell wall and the bentonite was a preferential path for water. In contrast, away from the bentonite column ends, the water content and dry density distributions through a given horizontal level were homogeneous. The degree of saturation tended to decrease from the hydration surface to the top of the block, but the values kept in a narrow range between 95 and 99 %.

| SLICE | Distance to hydration (cm) | *w* (%) | *w* ext (%) | *w* mid (%) | *w* int (%) | *w* isolines (%) |
|---|---|---|---|---|---|---|
| 1B | 13.45 | 29.6 | 29.9 | 29.2 | 28.8 | 29.6 |
| 2B | 11.45 | 29.4 | 29.4 | 29.3 | 29.1 | - |
| 3B | 9.45 | 29.4 | 29.3 | 29.5 | 29.6 | - |
| 4BP | 7.23 | 29.1 | 29.0 | 29.3 | 29.2 | 29.1 |
| 5P | 5.00 | 29.2 | 29.1 | 29.3 | 29.1 | - |
| 6P | 3.00 | 30.3 | 30.3 | 30.3 | 30.3 | - |
| 7P | 1.00 | 33.6 | 34.3 | 32.7 | 32.4 | 33.7 |
| Average | - | 30.0 | 30.2 | 30.0 | 29.8 | - |

*Table 7. Water content measured in subsamples according to their position (ext: average of 4 measurements at 6.1 cm from the axis, mid: average of 4 measurements at 3.4 cm from the axis, int: measurement at the axis)*

| SLICE | Distance to hydration (cm) | $\rho_d$ (g/cm$^3$) | $\rho_d$ ext (g/cm$^3$) | $\rho_d$ mid (g/cm$^3$) | $\rho_d$ int (g/cm$^3$) | $\rho_d$ isolines (g/cm$^3$) |
|---|---|---|---|---|---|---|
| 1B | 13.45 | 1.49 | 1.48 | 1.51 | 1.51 | 1.49 |
| 2B | 11.45 | 1.50 | 1.50 | 1.50 | 1.50 | - |
| 3B | 9.45 | 1.50 | 1.50 | 1.50 | 1.50 | - |
| 4BP | 7.23 | 1.51 | 1.52 | 1.51 | 1.51 | 1.51 |
| 5P | 5.00 | 1.52 | 1.52 | 1.51 | 1.51 | - |
| 6P | 3.00 | 1.49 | 1.49 | 1.49 | 1.48 | - |
| 7P | 1.00 | 1.43 | 1.41 | 1.44 | 1.45 | 1.42 |
| Average | - | 1.49 | 1.49 | 1.49 | 1.49 | - |

*Table 8. Dry density measured in subsamples according to their position (ext: average of 4 measurements at 6.1 cm from the axis, mid: average of 4 measurements at 3.4 cm from the axis, int: measurement at the axis)*

| SLICE | Distance to hydration (cm) | $S_r$ (%) | $S_r$ ext (%) | $S_r$ mid (%) | $S_r$ int (%) | $S_r$ isolines (%) |
|---|---|---|---|---|---|---|
| 1B | 13.45 | 95 | 95 | 96 | 95 | 95 |
| 2B | 11.45 | 96 | 96 | 96 | 95 | - |
| 3B | 9.45 | 96 | 95 | 97 | 97 | - |
| 4BP | 7.23 | 97 | 97 | 97 | 97 | 97 |
| 5P | 5.00 | 98 | 98 | 97 | 97 | - |
| 6P | 3.00 | 98 | 98 | 98 | 96 | - |
| 7P | 1.00 | 99 | 98 | 99 | 98 | 99 |
| Average | - | 97 | 97 | 97 | 97 | - |

*Table 9. Degree of saturation measured in subsamples according to their position (ext: average of 4 measurements at 6.1 cm from the axis, mid: average of 4 measurements at 3.4 cm from the axis, int: measurement at the axis)*

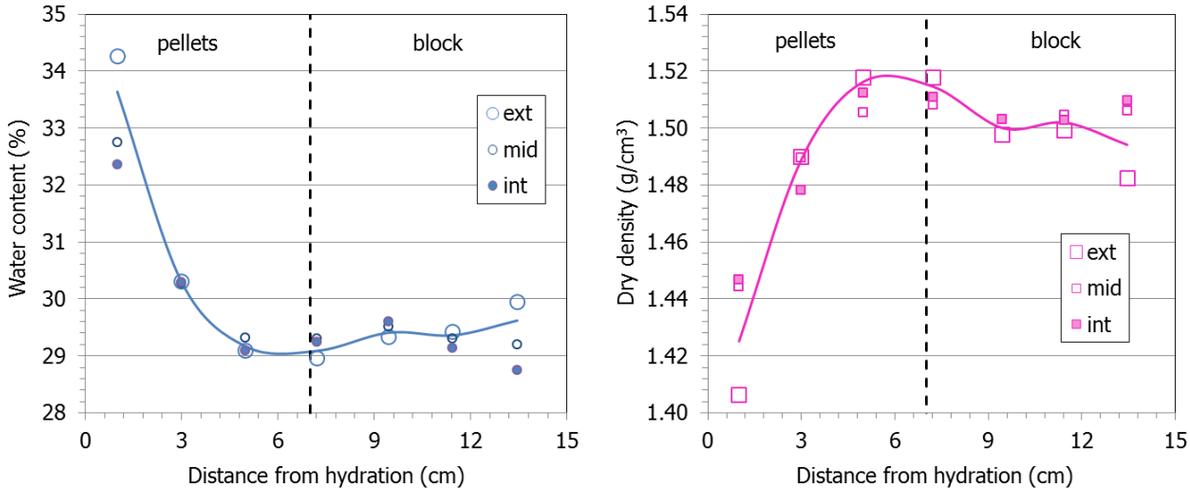


*Figure 37. Water content and dry density measured across the sample (ext: average of 4 measurements at 6.1 cm from the axis, mid: average of 4 measurements at 3.4 cm from the axis, int: measurement at the axis)*

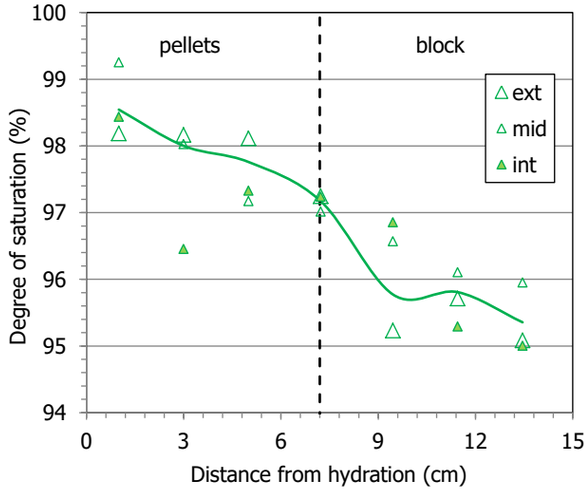


*Figure 38. Degree of saturation measured across the sample (ext: average of 4 measurements at 6.1 cm from the axis, mid: average of 4 measurements at 3.4 cm from the axis, int: measurement at the axis)*

Isolines were interpolated between these values, and 2D graphs of different sections across the column were obtained with Surfer (Golden Software Inc.) (see Appendix IV). In Figure 39 the water content and dry density distribution of a vertical section across diameter Y (perpendicular to the diameter where the sensors were placed) can be seen. The Figure highlights the higher water content at the bottom and at the external ring of the top as well as the inverse correlation with dry density. The software used to draw these graphs allows computation of mean values of the different parameters. Some of them are also included in the Tables above, and perfectly agree with those obtained by weighted average of all the measurements for a given area.

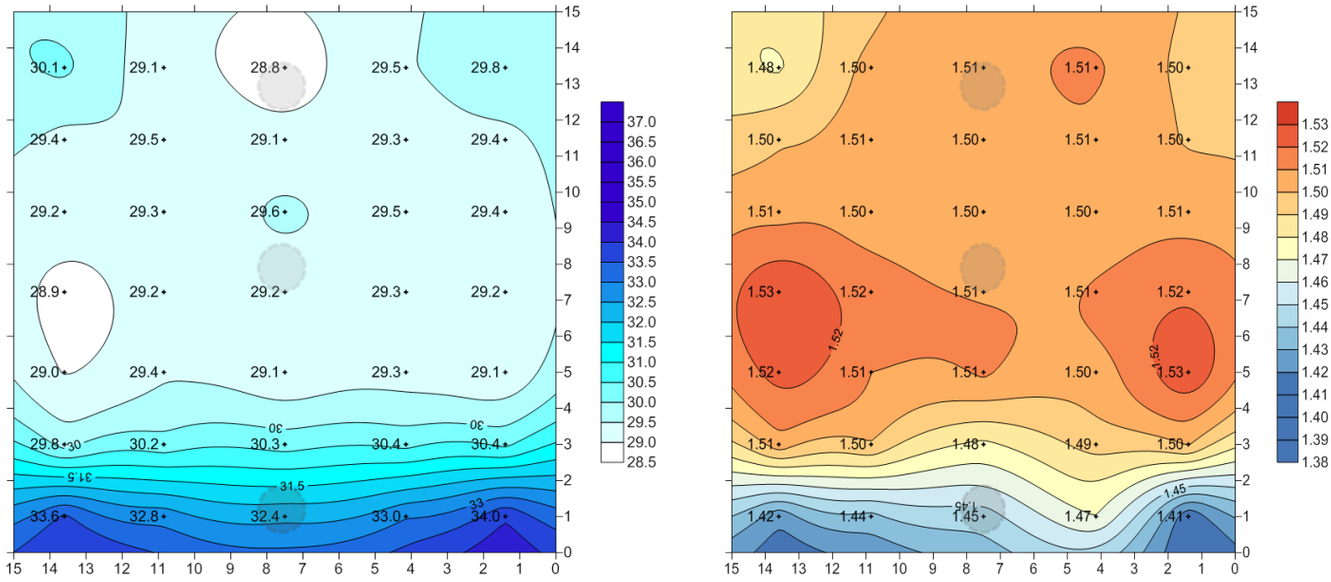


*Figure 39. 2D contour representations of water content (%, left) and dry density (g/cm³, right) of the vertical section along the Y diameter (see Figure 32 for location). The position of the RH/T sensors is indicated with shadowed circles*

## 8.2 PORE SIZE DISTRIBUTION AND SPECIFIC SURFACE AREA

### *8.2.1 METHODOLOGY*

The pore size distribution of some of the subsamples from the intermediate ring of each section was determined by mercury intrusion porosimetry (MIP). This technique allows the determination of the pore size distribution by injecting mercury into the sample at different pressures while measuring the volume intruded. The pressure applied may be related to the minimum pore diameter intruded taking into account the characteristics of the fluid (Washburn equation). The ratio of the volume of mercury intruded (pore volume) to the applied pressure (which conditions the minimum pore diameter) allows distribution curves to be obtained establishing the percentage of pores of a size included within a given interval.

The pores of the sample have to be empty, i.e. free of water, before the mercury intrusion test. In order to minimise the alteration of the clay microstructure during water removal, the samples were put in the ice condenser of a Telstar LioQuest equipment at -30°C for 3 hours. Subsequently, they were lyophilised for 22 hours at a temperature of -50°C under a vacuum of 0.2 mbar, so that to eliminate the water in the pores by sublimation. Thereafter, they were heated at 25-30°C for 3 hours. The samples were later kept in a desiccator until the MIP analysis. The porosimeter used was a Micromeritics AutoPore Series IV 9500, which allowed the exploration of pore diameters between 0.007 and 600 µm. Prior to mercury injection the sample was outgassed by applying a vacuum of 50 µm-Hg. Afterwards the mercury injection pressure was increased from 2.7 kPa to 220 MPa in 109 steps. To determine the extrusion branch of the curve, the pressure was released in 56 steps down to a pressure of 68.6 kPa. A contact angle of mercury of 139° both on advancing and of receding on the clay surface was considered.

The nitrogen sorption isotherms were determined in an ASAP 2020 of Micromeritics. The samples were lyophilised (as for the MIP samples explained above) and ground in an automatic agate mortar for 3 minutes. Aliquots of between 0.8 and 1.8 g were degassed at 90°C for the time necessary to reach a vacuum of 50 µm Hg, which was kept for 10 min. Afterwards the samples were kept at 90°C under vacuum for 500 minutes. The isotherms obtained had 58 points, 35 in the range of relative pressures between 0.01 and 0.99 (adsorption) and 23 points in the range between 0.99 and 0.14 (desorption). The BET method (Brunauer et al. 1938) was applied in the range of $P/P_0$ 0.06-0.2 to compute the external specific surface area, i.e. the surface of the intra-aggregate and inter-aggregate voids but not that of the interlayer space. This value is a measure of the degree of coherent stacking of smectite platelets (Sposito 1992).

### *8.2.2 RESULTS*

Figure 40 shows the intrusion curves for MX-80 samples of the same characteristics (reference curves) as the initial conditions used in the cell (block and pellets/powder mixture, see Table 3 for a reminder of the initial conditions of both materials). For the block part, the curve corresponding to a sample compacted at dry density 1.5 g/cm$^3$ with a water content of 9 % was used as representative of the initial state. For the GBM, a mixture of pellets/powder with a ratio 70/30 was prepared in the sample holder and slightly pressed. Although the density reached was much lower than the actual dry density of the mixture in the test (0.75 vs. 1.5 g/cm$^3$) the curve obtained probably displays the main features of the pore size distribution of the mixture. The Figure also shows the pore size distribution corresponding to single pellets with no powder addition. Obviously, the porosity of the high-density pellets was much lower, with barely no porosity corresponding to pores of size larger than 100 nm. The distribution for pore sizes below ~10 µm was similar for the pellets and for the mixture, but for larger pores there was a huge difference, since the individual pellets do not have large pores. The curve obtained for the mixture showed a predominant pore size around 150 µm (likely smaller for the actual mixture initial dry density).

Figure 41 shows the incremental curves of mercury intrusion for the subsamples of test CT31 as a function of the mean pore diameter of the diameter size intervals corresponding to each pressure increase step. The figure also includes the curves corresponding to the reference initial materials. Two major pore families could be identified, the separation between them being set at 200 nm, approximately separating macro and mesopores. As a result of hydration, the macroporosity of the block samples shifted to larger pore sizes but lower volumes, whereas the volume corresponding to pores smaller than 200 nm increased. The volume of macropores in the GBM decreased away from the hydration surface. For all the samples the mesopore mode size kept in values of 19±2 nm.

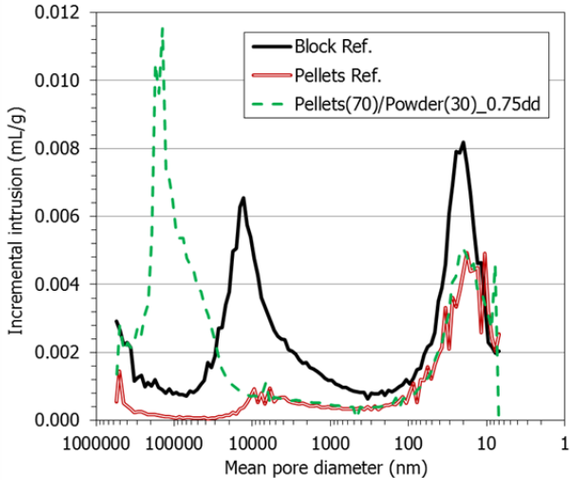


*Figure 40. Pore size distribution expressed as incremental mercury intrusion of initial materials used in test CT31*

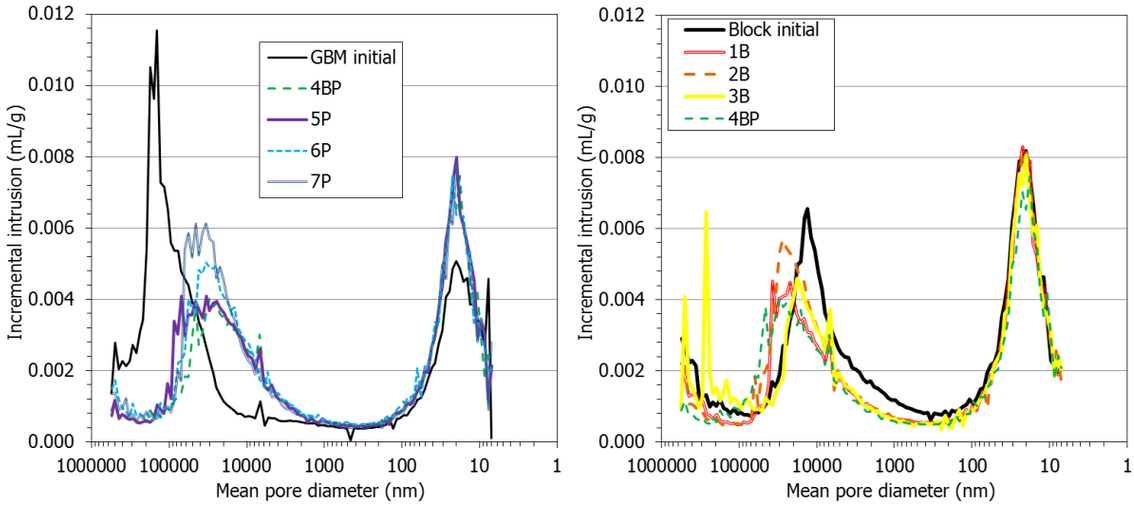


*Figure 41. Incremental mercury intrusion in subsamples from test CT31 and of the initial materials (see Figure 30 for the location of samples)*

The percentage of void ratio intruded, the void ratio corresponding to each pore size interval and the respective modes are shown in Table 10. The void ratio corresponding to each pore family for the different samples is shown in Figure 42 as a function of the distance to the hydration surface. As well, the mean sizes of the two pore families are shown on the right-hand side of the Figure. Overall, at the end of the test no significant differences between the block and the pellets/powder mixture parts could be observed, except that in the mixture part the void ratio corresponding to macropores was larger than in the block part, likely owing to the lower dry density of the mixture samples (Figure 37). Although the initial values for the pellets/powder mixture are uncertain, it is clear that both in the mixture and in the block, hydration entailed an increase in the void ratio corresponding to pores smaller than 200 nm and a decrease in the void ratio of the larger ones, particularly for the mixture.

| REF. | Distance to hydration (cm) | Intruded *e* (% of total) | *e* pores >200 nm (-) | Mode pores >200 (nm) | *e* pores <200 nm (-) | Mode pores <200 (nm) | BET $a_s$ ($m^2/g$) | *t*-plot µ-pore volume ($cm^3/g$) | $d_{001}$ (nm) |
|---|---|---|---|---|---|---|---|---|---|
| 1B | 13.45 | 71 | 0.309 | 35,233 | 0.532 | 21.0 | 34 | 0.004 | 1.527 |
| 2B | 11.45 | 76 | 0.349 | 25,729 | 0.492 | 18.9 | 35 | 0.004 | 1.552 |
| 3B | 9.45 | 74 | 0.336 | 250,894 | 0.505 | 18.9 | 32 | 0.004 | 1.563 |
| 4BP | 7.23 | 68 | 0.306 | 28,560 | 0.528 | 17.1 | 35 | 0.004 | 1.560 |
| 5P | 5.00 | 73 | 0.332 | 66,107 | 0.489 | 19.0 | 34 | 0.004 | 1.550 |
| 6P | 3.00 | 74 | 0.358 | 31,705 | 0.488 | 21.0 | 32 | 0.004 | 1.565 |
| 7P | 1.00 | 72 | 0.372 | 31,706 | 0.511 | 18.9 | 33 | 0.004 | 1.578 |
| Block | - | 83 | 0.396 | 12,362 | 0.457 | 19.0 | - | - | ~1.3 |
| Pellets | - | 88 | 0.072 | 5,517 | 0.238 | 17.1 | 31 | 0.004 | - |
| Powder | - | 24 | - | 205,617 | - | 19.0 | 25 | 0.004 | - |
| GBM | - | 24 | 2.375 | 135,332 | 0.318 | 18.9 | - | - | - |

*Table 10. Pore size distribution and BET specific surface area obtained with MIP and adsorption isotherms of samples from test CT31 (e: void ratio)*

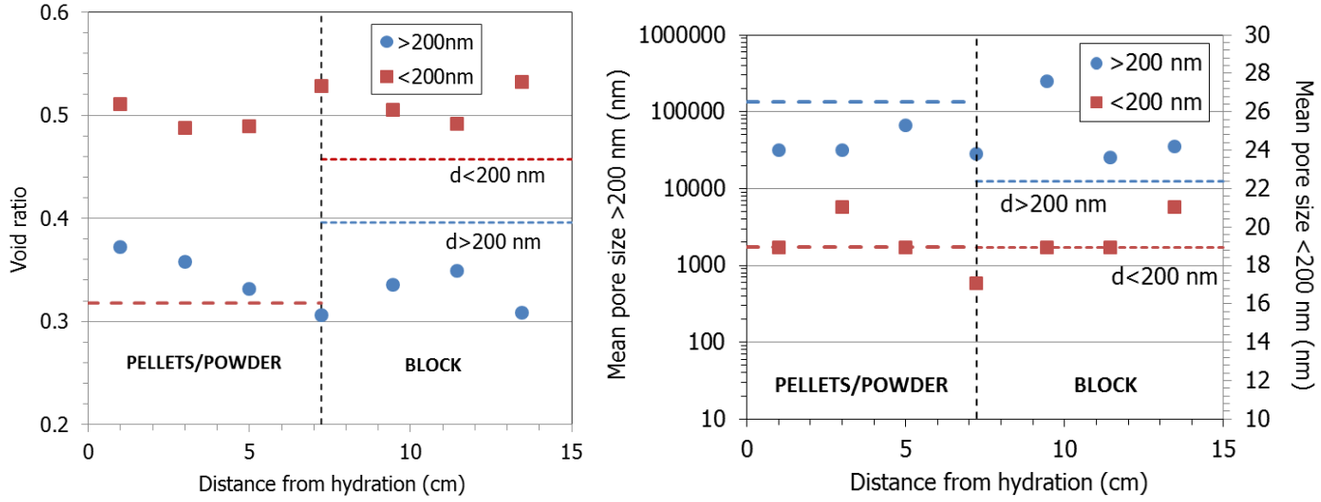


*Figure 42. Void ratio corresponding to different pore sizes (left) and mean pore size (right) obtained by MIP in samples from test CT31 (the thick horizontal lines indicate the values for the reference block and GBM; the initial macropore void ratio for the GBM was probably higher than 2, not shown in the Figure)*

The BET specific surface area of the samples was between 32 and 35 $m^2/g$ (Table 10), but these small variations were not related to the kind of sample or to their water content.

## 8.3 BASAL SPACING

### *8.3.1 METHODOLOGY*

The (001) reflection or basal spacing gives the distance along the crystallographic *c*-axis between clay lamellae, and for a given clay depends on the exchangeable cations present in the interlayer and their degree of hydration.

After dismantling, subsamples from each slice were preserved in paraffined foil and the X-ray profile of a plane surface of them was registered at laboratory temperature after removing the foil and without any further treatment. An anticathode of Cu (CuKα) radiation was used with a Philips model X'Pert-MPD diffractometer (Bragg Brentano configuration) at 40 mA, 45 kV operating condition. X-ray diffraction (XRD) experimental profiles were obtained with a fixed divergence slit size 0.6 mm, receiving slit size 5 mm and a scanning rate of 0.025 °2θ/s. Data were collected between 2 and 10°2θ. The goniometer settings were: automatic divergence slit and diffracted beam slit 2 mm. The position of the reflections was adjusted by using the quartz in the samples as an internal standard. The complete mathematical description of the scan pattern was obtained by combination of a polynomial function that describes the background and a profile function that fits the experimental reflections, in order to obtain better peak parameters (peak position, net intensity and full width at half maximum (FWHM)). The pseudo-Voigt profile function, which is the weighted mean between a Lorentz and a Gaussian function, was used to fit the reflections as well as to deconvolute overlapped peaks.

### *8.3.2 RESULTS*

The basal reflection was measured by XRD and the values obtained are plotted in Figure 43 (shown also in Table 10). The values were all in a narrow range between 1.58 and 1.52 nm, corresponding to the two-layer hydration state. Overall they were higher for the pellets/powder mixture samples, but in both parts, mixture and block, they were higher towards the hydration surface. The Figure shows also the direct correlation between the basal spacing and the water content. The samples were X-rayed 5 days after dismantling, which could have allowed certain water redistribution in the microstructure.

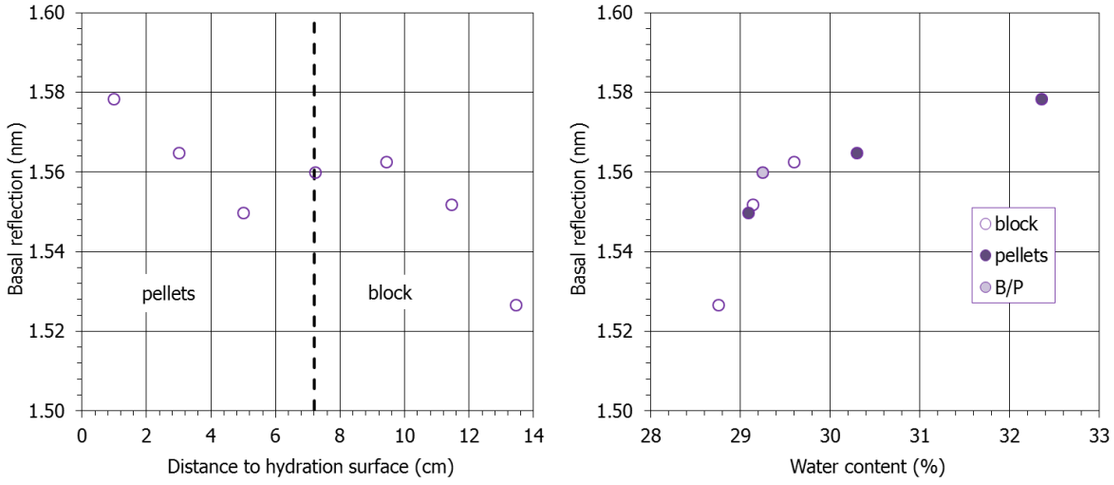


*Figure 43. Main diffraction reflection of the basal spacing of subsamples of test CT31 as a function of their position inside the cell (left) and their water content (right)*

## 8.4 OPTICAL ANALYSIS AND TOMOGRAPHY

To get some additional insights into the microstructure of this material, samples taken from slices 1B, 7P and 4BP, corresponding to the compacted block, the pellets mixture, and the contact between both, respectively, were observed with a stereo microscope and analysed by X-ray microcomputed tomography (Figure 44). These samples were taken from areas with similar location with respect to the axis of the bentonite column, specifically from the areas designated as 1º quadrants in Figure 32, right. The samples for MIP and basal spacing analyses were taken from the same areas, what allows a closer comparison between properties. In particular the samples were taken from the quadrants 1B-1º, 7P-1º and 4BP-1º, where dry density and water content were also checked (Table 11).


*Figure 44. Example of subsamples for stereo microscope and computed microtomography observations, corresponding to quadrant 1B-1º (upper surface (left), lateral view (middle) and bottom surface (right) of the subsamples)*

| SAMPLE | $\rho_d$ (g/cm$^3$) | $w$ (%) | $S_r$ (%) | $w^a$ (%) |
|---|---|---|---|---|
| 1B-1º | 1.48 | 29.3 | 93 | 25.8 |
| 4BP-1º | 1.53 | 28.2 | 96 | 24.7 |
| 7P-1º | 1.45 | 32.2 | 99 | 28.0 |

[a] values after tomography

*Table 11. Characteristics of the samples used for microscopy and tomography analyses*

### *8.4.1 STEREO MICROSCOPE ANALYSIS*

The stereo microscope used was a Nikon SMZ 1500, with a zoom range between 0.75x and 11.25x, a zoom ratio of 15:1 and with tree external illuminators SCHOTT KL 1500 LCD. It was connected to an Eakins FHD Camera v 2.0 of 21 Megapixels and to a computer.

To the naked eye and under the stereo microscope the samples showed a high degree of homogeneity, and the contact between block and pellets/powder mixture was diffuse. For a better appreciation of the different mineral grains, the sample was cut by fracturing it, since the cut generated by a knife or saw tended to generate

observation surfaces of poor quality, due to the dragging and deformation of the more plastic particles. The observations were carried out both on the surface parallel to the horizontal plane and the surface perpendicular to this plane, considering these planes according to the disposition of the bentonite cylinder during the test. In the case of the part of the bentonite column corresponding to the block (slice 1B), the horizontal plane corresponds to the compaction surface.

Figure 45 shows the three surfaces corresponding to the horizontal plane of samples 1B, 4BP and 7P (Figure 44, left). The horizontal plane was generated during the sawing of the vertical slices, except for sample 1B (Figure 31, left), which is the reason why the image of the grains is blurred, and the visible porosity conditions may have been distorted by dragging, local compaction, or any other process associated with the cutting of the sample. In any case, the image corresponding to the block area (left) seems sharper, with even a macropore visible (top left in 1B). The mixture zone (right), however, looks more homogeneous and blurred, possibly because of its higher water content and degree of saturation. Regarding the contact zone between block and mixture, the interface could not be defined.

*Figure 45. Aspect under the stereo microscope of the surface corresponding to the horizontal plane of samples 1B (left), 4BP (middle) and 7P (right). The (approximate) spacing between the dark-coloured lines is 0.5 mm*

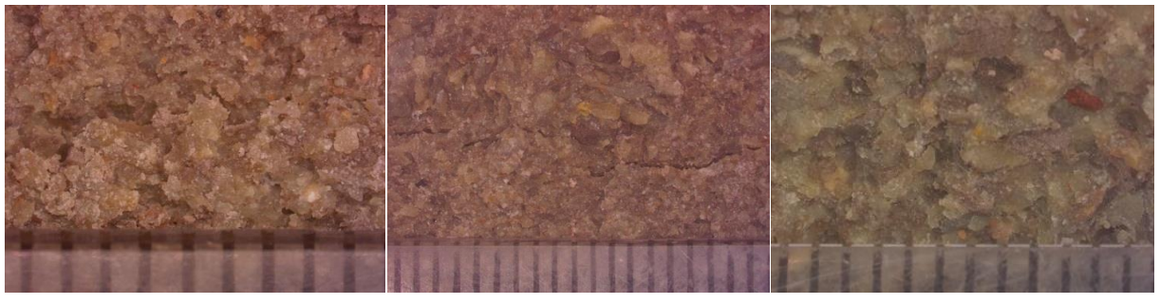

*Figure 46. Aspect under the stereo microscope of the surface corresponding to the lateral plane of samples 1B (left), 4BP (middle) and 7P (right). The (approximate) spacing between the dark lines is 0.5 mm*

Figure 46 shows the images corresponding to the perpendicular plane of the samples shown above (Figure 44, middle). The sharpness of the grains in these images was higher because they had not been deformed by the effect of the cutting of the samples. The interface between the block and the mixture can be seen more clearly. The greenish hue of the mixture zone corresponds to the most hydrated section (right), where no visible

porosity is observed at this scale. The compacted block (left), shows a more brownish hue and some visible pores. This contact is a zone of weakness that generated (possibly during observation because of slight drying) the formation of a small fracture separating a zone of more irregular and slightly larger grains (upper part of the central image, mixture) from another one of more homogeneous sizes (bottom, block).

In general terms, at this scale the separation between pellets and block is subtle, given the degree of homogeneity achieved, with a very reduced presence of observable pores in both cases.

### *8.4.2 MICROCOMPUTED TOMOGRAPHY*

Micro-computed tomography is an X-ray image technique that makes it possible to scan, explore and model samples in 3D. It is a non-destructive technique which allows the virtual reconstruction of the sections of an object based on images (radiographies) acquired over 360°. The equipment used at the CENIEH facilities (Burgos, Spain) is a MicroCT V|Tome|X s 240 by GE Sensing & Inspections Technologies Phoenix X-Ray. The maximum diameter and length of the sample to be scanned in 3D is 200 mm x 400 mm, with a maximum weight of 10 kg. It consists of a 240 kV X-ray tube with detectability values of 1 µm (microfocus), and a 180 kV tube (nanofocus), with detectability values below 0.5 µm. However, in the case of the samples from test CT31 only those elements with a size ≥25 µm could be detected, because of the large size of the samples analysed.

Images of the samples were taken over a period of 1.5 h per sample. During the process the samples were slightly dried, and the final values of water content are shown in Table 11. The images were processed with the Dragonfly software, which selects ranges of a grey scale. The grey values are related to the density of the element, with lighter areas representing denser materials and black areas corresponding to voids. However, the contrast between the grey of pores and matrix was not enough as to allow an accurate segmentation of pores, which had to be done with a trained mathematical model (San Miguel 2022). Artefacts were later manually corrected. Examples of these images are shown in Figure 47. They all look homogeneous, although maybe the image of the pellets mixture (right) contains larger particles than the image of a block sample (left). Molinero-Guerra et al. (2018) followed the saturation of a mixture of pellets and powder of MX-80 bentonite by X-ray CT and concluded that, upon saturation, the material presented an apparent homogeneity with nearly all air voids closed. In the image of the middle sample, the interface between block and pellets is only subtly indicated. In contrast, the 3D reconstruction of the BP sample clearly shows the interface between both parts as an area with lower porosity (Figure 48). A dedicated study was performed to rule out artefacts in this reconstruction. These 3D reconstructions also highlighted the different porosity of the two components and areas of different porosity inside them. The software allows a quantification of porosity and connectivity. Indeed, the term porosity is used here in the sense of “macroporosity”, since only pores larger than 25 µm could be told apart. Consequently, the porosity values obtained (disregarding desiccation cracks) were very low:1.2 % for the block part, 0.8 % for the pellets part, and 1.5 % for the BP interface. No trends in the pore connectivity were detected.

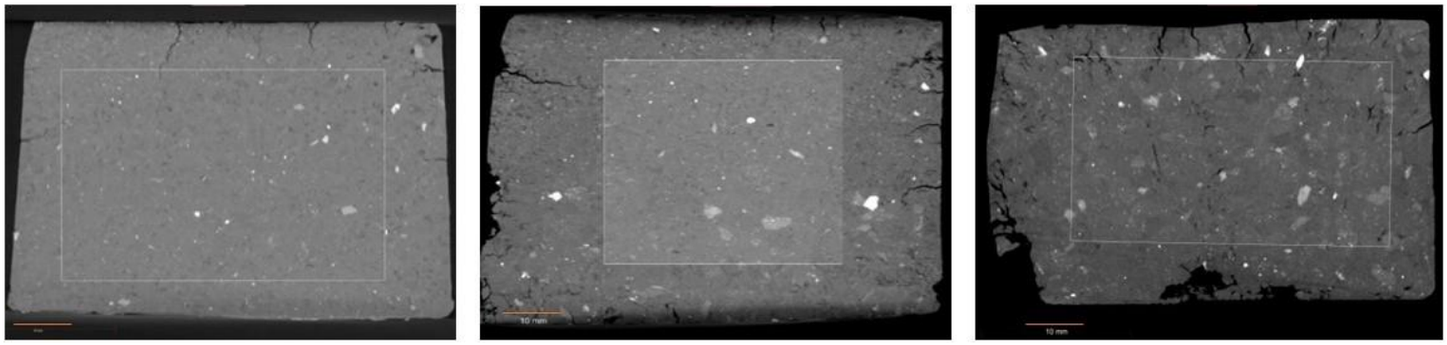

*Figure 47. Image of samples 1B (left), 4BP (middle, block part on top) and 7P (right). The bars are ~10 mm long*

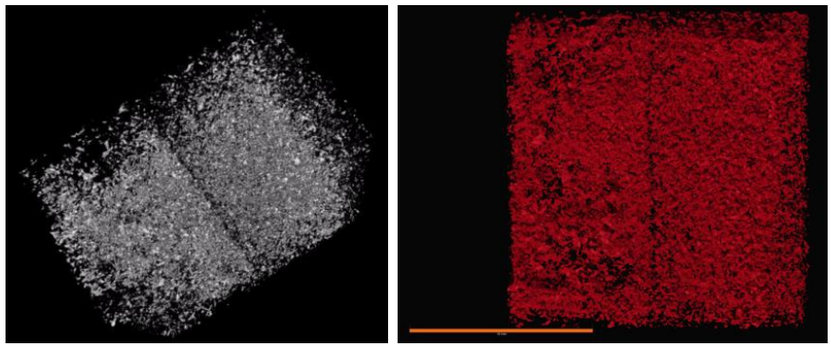

*Figure 48. 3D reconstruction of the 4BP sample (the block is on the right hand side in both images, the bar size is 10 mm)*

# 9 SUMMARY AND DISCUSSION

The test presented allowed to follow the hydro-mechanical evolution of a two-component (block and pellets/powder mixture, GBM) buffer material upon hydration under isochoric conditions at ambient temperature. The initial dry density of the two components was the same and the water contents were not too different. Both parts were manufactured from Wyoming-type bentonite. Hydration took place from the bottom, through the pellets part. During the test, the relative humidity and radial pressure were measured at three different levels as well as the pore pressure on top.

The initial water intake was very quick, because of the high permeability of the pellets/powder mixture. In fact, the relative humidity sensor placed at 13 mm from the hydration surface was flooded in a few hours, the RH middle sensor started to record increases after just 1 day of hydration and the top RH sensor after 10 days. After 2 years of hydration, consistently with the stabilisation of water intake, the RH at all positions inside the bentonite was around 100 %.

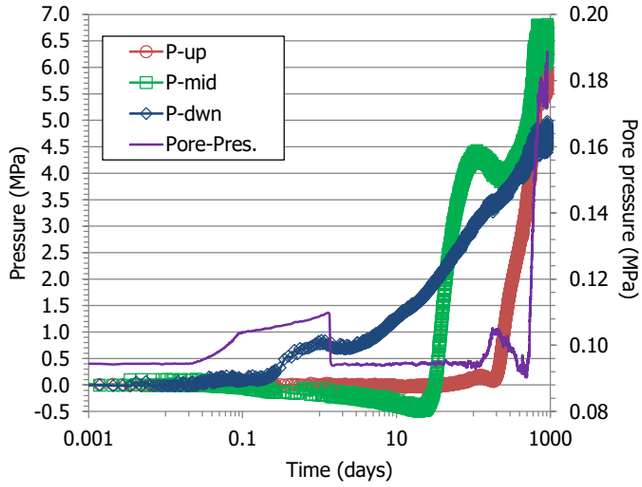


*Figure 49. Radial pressure and pore pressure evolution during hydration in test CT31*

The radial pressure development was related to the water intake, and hence was very quick at the bottom, where some collapse took place (attested by a soft decrease of the radial pressure). The collapses in the mixture part were subsequently transferred to the middle part of the cell, where the radial stress also experienced a soft decrease prior to the sharp initial increase, which was followed by a soft decrease and a subsequent continuous, but not lineal, increase until stabilisation (Figure 21 and Figure 49). In the top part of the cell, where the block was placed, no stress changes were recorded for a long time (200 days), but then the stress increase was steady until stabilisation. The pressure stabilisation took place sequentially, starting by the bottom sensor and ending with the pore pressure measured on top. The left part of Figure 50 focuses on the time period over which pressures stabilised, with an indication of the approximate moment when it happened for each sensor, between days 620 and 740. These times are plotted as a function of the location of the sensors on the right hand of the Figure.

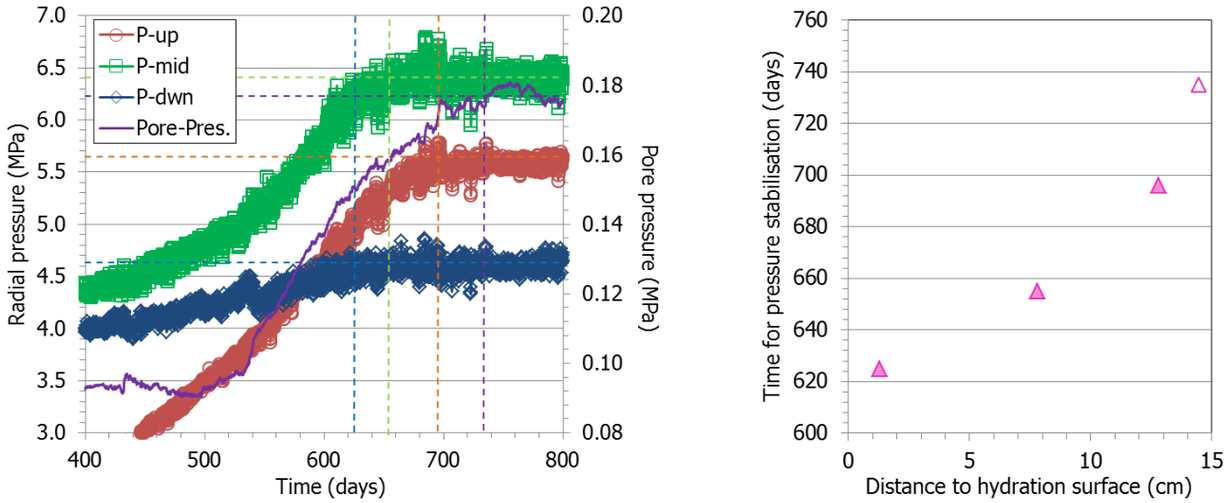


*Figure 50. Stabilisation of lateral and pore pressure during the hydration phase of test CT31*

The relation between the relative humidity and stress changes at a given location (Figure 51) shows that, except for the sensor closest to the hydration surface, which became quickly flooded, the middle and top pressure sensors recorded the largest pressure increases when the overall degree of saturation was higher than 90 % (after ~400 days of hydration). In particular the middle sensor, located in the block part at 8 cm from the hydration surface, recorded an increase in pressure from 4 to 7 MPa for a relative humidity increase of only 4 % (from 96 to 100 %). This can be better observed on the right hand part of the Figure 8 and 13 cm from the hydration surface the sharpest pressure increase took place when the relative humidity was higher than 98 %. In the EB in situ test performed at the Mont Terri URL, where a large-scale two-component barrier (FEBEX GBM and blocks) was tested for 10.5 years, most of the sensors installed in the bentonite recorded relative humidity values of 100 % only one year after the beginning of the test, whereas it took four years for the total pressure sensors to record stable values that kept approximately constant until the end of the test (García-Siñeriz et al. 2015). This was interpreted by Villar et al. (2021) as a demonstration that the redistribution of water in the microstructure was the mechanism that triggered most of swelling. In the case of sodic bentonites, such as MX-80, it is known that osmotic swelling, which is particularly relevant when the degree of saturation is very high, may be the largest component of swelling, overcoming the crystalline one. This would be confirmed by the fact that the basal spacings measured upon dismantling corresponded only to the 2-layer hydrate (Figure 43), despite the high degree of saturation (see below).

Hydration tests performed in large-scale cells where axial and radial pressures were measured at different heights along the sample length showed that during saturation, the transient pressure values were related to the local dry density (Dueck et al. 2016, Bian et al. 2019, Bernachy-Barbe et al. 2020, 2022, Harrington et al. 2020). Upon dismantling of the CT31 test the final dry density of the bentonite was determined at numerous locations (Figure 37). Thus, the final equilibrium pressures measured at three different levels (shown in Figure 50) could be related to the final dry densities measured in the area where the sensor was located (Figure 52). The highest stress (and hence, dry density) corresponded to the middle part of the sample. The empirical exponential correlation between dry density and axial swelling pressure obtained from tests in standard

oedometers in which MX-80 samples compacted to different dry densities were saturated with deionised water (Equation 1) is also plotted in the Figure. From this Equation the axial swelling pressure corresponding to an MX-80 bentonite compacted to the overall dry density of the CT31 sample (1.50 g/cm$^3$) would be 3.4 MPa. An evaluation of the relationship between dry density and swelling pressure for the WH2 bentonite (from which the pellets used in this research were manufactured) reported by Bosgiraud a& Foin (2016) showed that with a dry density of 1.50 g/cm$^3$ the swelling pressure obtained at saturation of material would be around 4 MPa. These values are considerably lower than those actually measured in test CT31, but they correspond to axial pressures, whereas in the cell only radial pressures were measured. In a hydration test performed with a bentonite pellets/powder mixture, the axial swelling pressure measured was mostly lower than the radial pressures, although the authors hypothesised that the reason could be a lower average dry density at placement at the upper surface where the axial pressure was measured (Bernachy-Barbe et al. 2020). Authors working with compacted bentonite or sand/bentonite mixtures generally found that radial pressures were lower than axial pressures, but that the difference between both decreased as full saturation was approached and for high-density samples and high pressures (Pintado et al. 2013, Saba et al. 2014, Lu et al. 2021). An additional reason for the higher than expected pressures measured could be the scale effect, since previous laboratory work showed that the swelling pressure tends to be higher as the testing cell is larger (Imbert & Villar 2006).

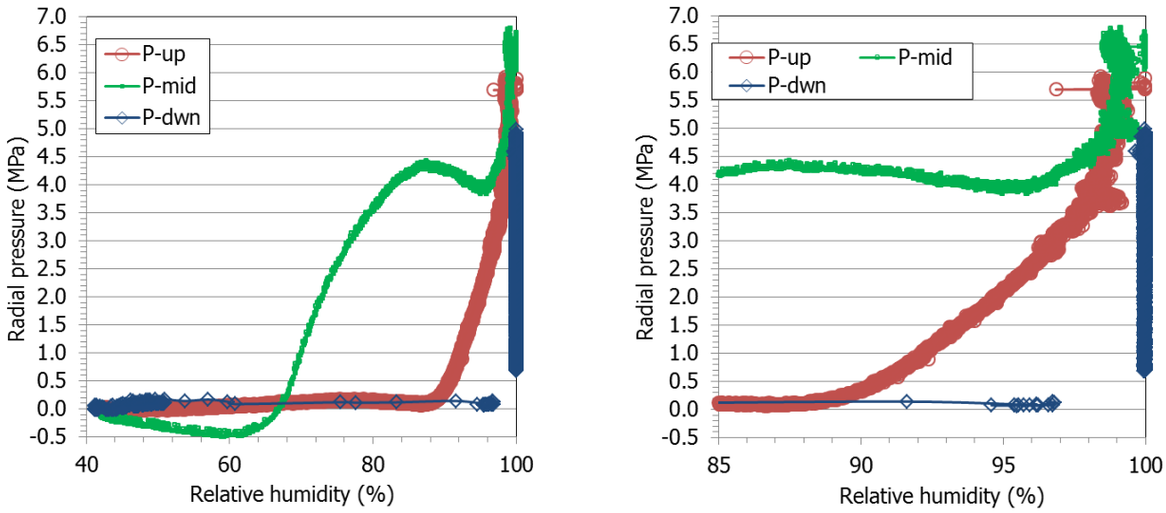


*Figure 51. Radial pressure measured at different heights in test CT31 against the relative humidity in the same locations (see Figure 2 for location of sensors)*

The tests performed by Martikainen et al. 2018 (reported in Talandier, 2019) were very similar in design and dimensions to the tests presented here (except that the block and the pellet mixture had very different initial dry densities), with hydration under an injection pressure of 10 kPa taking place through the pellets, which were placed on top. In those tests, MX-80 bentonite was also used and the radial pressure developed by the block and the pellets parts were measured in addition to the axial ones. The axial and radial pressure development in the areas farther away from hydration (i.e. around the block part) displayed the initial peak followed by a decrease and a smooth eventual increase, and were lower in the axial direction than in the radial one. These

measurements also showed significantly lower pressures in the pellets than in the block part. The modelling groups involved in a benchmark where these tests were analysed, concluded that this difference was due to the initial contrast of density between the top and bottom of the sample but also to the friction between the bentonite and the steel cell wall (Talandier 2019). However, in test CT31, in which the density of the two components was initially similar, lower pressures were measured in the pellets part.

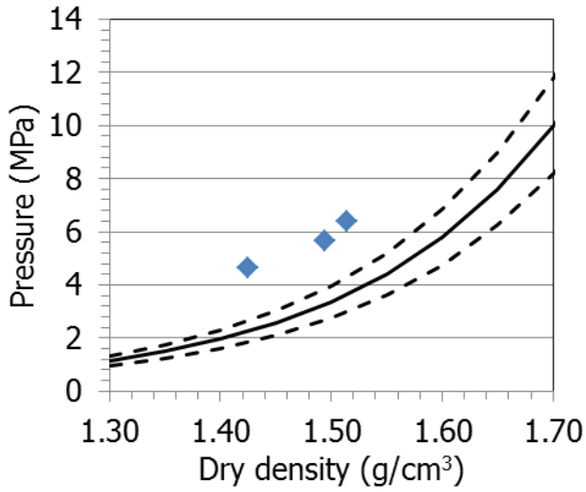


*Figure 52. Axial swelling pressure of MX-80 compacted to different dry densities (curves, Eq. 1) and equilibrium radial pressures measured in test CT31 as a function of the final dry density measured at the sensors' locations (symbols)*

At the end of the test, most of the bentonite had water contents between 29 and 30 % and dry densities between 1.49 and 1.52 g/cm$^3$, but the bentonite at less than 3 cm from the hydration surface (pellets/powder mixture) presented significantly higher water contents and dry densities (Figure 37), even though the initial dry density of the block and the mixture parts were similar and hydro-mechanical equilibrium had been reached. This would indicate that the source of final heterogeneity was not the initial state, but the hydration process itself. In the series of hydration tests of binary samples reported in Villar et al. (2021), no complete homogeneity in terms of dry density or water content was reached in any case, even after full saturation: the water content decreased from the hydration surface to the opposite end whereas the dry density increased. These heterogeneities resulted from the initial swelling and ensuing density decrease of the bentonite that became first saturated (those parts closest to the bottom hydration surface), and the consequent compression of the bentonite located upwards. Similarly, Bernachy-Barbe et al. (2020) found analogous water content and dry density distributions at the end of a test performed with a similar pellets/powder mixture, after 1200 days of hydration.

Despite the fact that no further water intake or pressure changes were recorded in test CT31, the final measured degrees of saturation were lower than 100 % (between 95 to 99 %) and tended to decrease away from the hydration surface (Figure 38). The samples likely experienced expansion upon extraction from the cell and later trimming, as well as some drying during manipulation, which would explain the degrees of saturation <100 %. Once overall full saturation was reached, no further water content or dry density changes are to be

expected, which would mean that part of the initial volume changes were irreversible. The mixture/block interface did not seem to have had any effect on the continuous gradients observed, i.e. there were no sudden changes across the interface.

Concerning the microstructural modifications during hydration, the BET specific surface area of the samples was between 32 and 35 $m^2/g$, but these small variations were not related to the kind of sample or to its water content. As well, most parameters inferred by MIP (volume and size of each pore range, ratio between them), were similar for the two kinds of samples (pellets/powder mixture and block), except that close to the hydration surface the void ratio corresponding to macropores was larger than in the block part, likely owing to the lower final dry density of the mixture. As a result of hydration, the volume of micropores increased with respect to the initial one in all the bentonite, particularly in the case of the mixture. The increase in the volume of micropores was likely related to the increase in the smectite basal spacing as a result of the hydration of the interlayer cations. In fact, the basal reflection values were all in a narrow range between 1.58 and 1.52 nm, related to the water content, but corresponding in all cases to a predominant 2-layer hydration state. However, the basal spacings obtained in block and GBM samples of FEBEX bentonite saturated under similar conditions were considerably higher (Figure 53), corresponding for the GBM samples to the 3-layer hydrate (Villar et al. 2021). This could be an indication of the lower relevance of the crystalline swelling in the sodic MX-80 bentonite, which had interlayer cations with a lower degree of hydration, despite the fact of being fully saturated and having developed a high swelling pressure. Both in the FEBEX and the MX-80 bentonites the basal spacings were higher for the pellets samples, which had higher water contents and lower dry densities, particularly in the case of the tests performed with FEBEX bentonite.

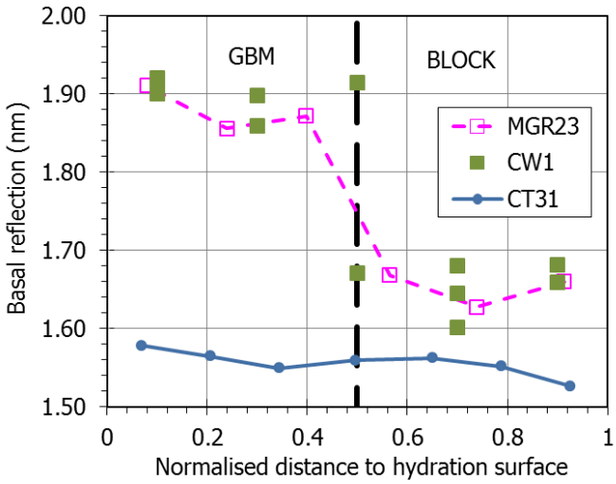


| SAMPLE | BENTONITE | Duration (days) | Dry density ($g/cm^3$) | Degree of saturation (%) |
|---|---|---|---|---|
| MGR23 | FEBEX | 210 | 1.43 | 101 |
| CW1 | FEBEX | 379 | 1.45 | 113 |
| CT31 | MX-80 | 922 | 1.49 | 100 |

*Figure 53. Main diffraction peak of the basal reflection of subsamples of tests MGR and CW (FEBEX bentonite, length of 10 cm in tests MGR and 12 cm in CW, Villar et al. 2021) and CT31 (MX-80 bentonite, length 15 cm). The Table on the right hand indicates the duration of the tests and the final average values for the binary sample (block+mixture)*

The basal reflection measurements performed in samples of MX-80 bentonite with different water contents and dry densities (Villar et al. 2012 and unpublished results), show that for water contents around 30 %, values of between 1.54 and 1.85 nm can be expected. Hence, the CT31 samples would be in the lower range of these values (Figure 54), which could be because the samples were X-rayed 5 days after dismantling.

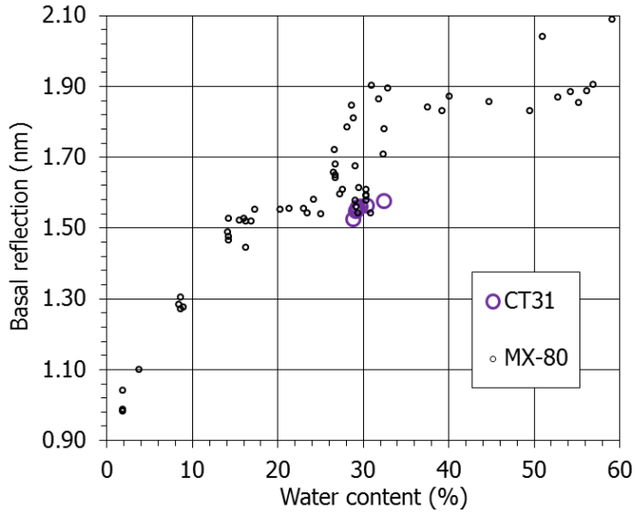


*Figure 54. Main diffraction peak of the basal reflection of subsamples of lab tests performed with MX-80 bentonite (values from Villar et al. 2012 and other unpublished results) and of the CT31 test*

# 10 CONCLUSIONS

The hydro-mechanical evolution of a two-component bentonite buffer material –a pellet/powder mixture and a compacted block– was studied by means of a laboratory hydration test performed under isochoric conditions. The test was performed in an instrumented cell (15x15 cm) with MX-80 bentonite (test CT31). The dry densities of the block and the mixture parts were initially similar. Radial pressures and relative humidity were measured at different locations. Hydration took place through the mixture part, placed at the bottom of the cell, under a low water injection pressure. The test was dismantled after having reaching relative humidity and pressure stabilisation and full saturation (922 days).

The analysis of the results obtained allowed to draw the following conclusions:

- Because of their low density and large macroporosity, hydration through the pellets was initially quick, even though the water injection pressure was very low.

- The radial pressure development was not continuous, and was linked to the increase in relative humidity. After a first sharp increase when the water front arrived, there was an intermediate period of pressure stabilisation or even decrease, indicating the collapse of the macrostructure. Only when the overall degree of saturation was very high, the pressure increased again until its final equilibrium value. This pressure development pattern had been previously observed also in samples of compacted bentonite and of pellets.

- The pore pressure build-up on top of the cell was also related to the full saturation of the bentonite in the upper part of the cell.

- The radial pressures measured were exponentially related to the dry density of the bentonite in the area where the sensors were placed. Hence, the equilibrium pressure in the middle part of the binary sample was higher than that at the bottom and on top, in relation with the dry density distribution. In all cases the pressures measured were higher than what could be expected according to the empirical correlation obtained between pressure and dry density from tests in standard oedometers performed with MX-80 bentonite powder compacted at different dry densities.

- Although the initial dry density and water content were similar in the pellets and the block parts, inhomogeneities persisted after full saturation and pressure stabilisation, with higher water content and lower dry density in the proximity of the hydration surface. The shapes of the water content and dry density gradients were not affected by the mixture/block interface.

The pore size distribution after saturation as determined by MIP was similar for the mixture and the block, since a significant reduction in the volume and size of the macropores took place in the pellets/powder mixture part. In both parts there was a substantial increase in the volume of pores smaller than 200 nm and in the basal spacing of the smectite (which is an indication of the number of water layers in the interlayer), even though the basal spacing was higher in the pellets/powder mixture.

# 11 REFERENCES


[1] ANDRA 2013. The Cigéo Project – "Meuse/Haute-Marne Reversible Geological Disposal Facility for Radioactive Waste" - Project Owner File Public Debate of 15 May to 15 October 2013.

[2] Bernachy-Barbe, F. 2021. Homogenization of bentonite upon saturation: Density and pressure fields. Applied Clay Science 209. pp 106122. https://doi.org/10.1016/j.clay.2021.106122

[3] Bernachy-Barbe, F., Conil, N., Guillot, W., Talandier, J. 2020. Observed heterogeneities after hydration of MX-80 bentonite under pellet/powder form. Applied Clay Science 189. 105542. https://doi.org/10.1016/j.clay.2020.105542

[4] Bernachy-Barbe, F., Bosch, J.A., Campos, G., Carbonell, B., Daniels, K.A., Ferrari, A., Graham, C., Guillot, W., Gutiérrez-Álvarez, C., Harrington, J.F., Iglesias, R.J., Kataja, M., Kröhn, K.P., Kröhn, M., Mašín, D., Najser, J., Pingel, J.L., Real, E., Schäfer, T., Svodoba, J., Sun, H., Tanttu, J., Villar, M.V., Wieczorek, K. 2022. Experimental work on bentonite evolution in the frame of BEACON – final report of WP4. BEACON Deliverable D4.3. 237 pp.

[5] Bian, X., Cui, Y.J., Zeng, L.L., Li, X.Z. 2019. Swelling behavior of compacted bentonite with the presence of rock fracture. Engineering Geology 254. Pp 25-33. https://doi.org/10.1016/j.enggeo.2019.04.004

[6] Bosgiraud, J.M., Foin, R. 2016. Test report on FSS metric clayish material emplacement tests with clayish material definition and laboratory work on its performance. Project DOPAS Work Package 3 - Deliverable 3.7. European Commission Grant Agreement no. 323273, 35 pp. https://igdtp.eu/documents/

[7] Brunauer, S., Emmett, P.H., Teller, E. 1938. Adsorption of gases in multimolecular layers. Journal of the American Chemical Society 60. Pp 309–319.

[8] Conil, N., Talandier, J., Noiret, A., Armand, G., Bosrigaud, J.M. 2015. Report on Bentonite Saturation Test (REM). DOPAS Work Package 4 Deliverable D4.2. European Commission Grant Agreement no. 323273, 97 pp. https://igdtp.eu/documents/

[9] Darder, B., Tang, A.M., Pereira, J.M., Dangla, P., Roux, J.N., Chabot, B., Talandier, J., Vu, M.N. 2022. Influence of heterogeneities of density on the hydromechanical behaviour of pellet-based bentonite materials in imbibition experiments. Applied Clay Science 216. Pp 106353. https://doi.org/10.1016/j.clay.2021.106353

[10] Dueck, A., Goudarzi, R., Börgesson, L. 2016. Buffer homogenisation. Status report 3. Technical Report SKB TR-16-04. Svensk Kärnbränslehantering, Stockholm, 104 pp.

[11] ENRESA 2005. Engineered barrier emplacement experiment in Opalinus Clay for the disposal of radioactive waste in underground repositories. Final Report. Publicación Técnica ENRESA 02/05. Madrid, 101 pp.

[12] García-Siñeriz, J.L., Villar, M.V., Rey, M., Palacios, B. 2015. Engineered barrier of bentonite pellets and compacted blocks: state after reaching saturation. Engineering Geology 192. Pp 33–45. https://doi.org/10.1016/j.enggeo.2015.04.002.

[13] Gómez-Espina, R. & Villar, M.V. 2016. Time evolution of MX-80 bentonite geochemistry under thermo-hydraulic gradients. Clay Minerals 51(2). pp 145-160. DOI. 10.1180/claymin.2016.051.2.03

[14] Harrington, J.F., Daniels, K.A., Wiseall, A.C., Sellin, P., 2020. Bentonite homogenisation within engineered cavities: the evolution of swelling pressure during bentonite hydration. International Journal of Rock Mechanics and Mining Sciences 136, 104535. doi:10.1016/j.ijrmms.2020.104535.

[15] Imbert, C., Villar, M.V. 2006. Hydro-mechanical response of a bentonite pellets/powder mixture upon infiltration. Applied Clay Science 32. pp. 197-209. https://doi.org/10.1016/j.clay.2006.01.005

[16] Lu, Y., Ye W.M., Wang, Q., Zhu, Y.H., Chen, Y.G., Chen, B. 2021. Anisotropic swelling behaviour of unsaturated compacted GMZ bentonite hydrated under vertical stresses. Bulletin of Engineering Geology and the Environment 80.pp. 5515-5526.

[17] Martikainen, J., Pintado, X., Mamunul, H. 2018. Laboratory tests to evaluate bentonite homogenization. Internal memorandum POS-026579. Eurajoki, Finland. Posiva Oy.

[18] Molinero Guerra, A. 2018. Caractérisations expérimentale et numérique du comportement hydro-mécanique d'un matériau hétérogène : mélange de poudre/pellets de bentonite. Ph. Thesis. Université Paris-Est, 190 pp.

[19] Molinero Guerra, A., Cui, Y.-J., Mokni, N., Delage, P., Bornert, M., Aimedieu,Molinero-Guerra, A., Aimedieu, P., Bornert, M., Cui, Y.J., Tang, A.M., Sun, Z., Mokni, N., Delage, P. and Bernier, F. 2018. Analysis of the structural changes of a pellet/powder bentonite mixture upon wetting by X-ray computed microtomography. Applied Clay Science 165. 164-169.

[20] NAGRA 2019. Implementation of the Full-scale Emplacement Experiment at Mont Terri.: Design, Construction and preliminary results. NAGRA Technical Report NTB 15-02. Wettingen, 147 pp

[21] Pintado, X., Mamunul, H.M., Martikainen, J. 2013. Thermo-Hydro-Mechanical Tests of Buffer Material. Posiva Report 2012-49. Olkiluoto, 152 pp. ISBN 978-951-652-231-2.

[22] Saba, S., Barnichon, J.D., Cui, Y.J., Tang, A.M., Delage, P. 2014. Microstructure and anisotropic swelling behaviour of compacted bentonite/sand mixture. Journal of Rock Mechanics and Geotechnical Engineering 6(2). Pp.126-132.

[23] San Miguel, M. 2022. Análisis de microscopía y micro-tomografía. Informe MI-2022-0007. CENIEH, Burgos, 4 pp.

[24] Sellin, P. 2022. Full project report that includes the synthesis report from the WP1-6. BEACON Deliverable D7.8. 14 pp.

[25] Sposito, G. 1992. Characterization of particle surface charge. In. Buffle J, van Leeuwen (eds.). Environmental particles. Chelsea, MI. Lewis Publ. pp 291 – 314.

[26] Talandier, J. (Ed.) 2019. Synthesis of results from task 5.1. BEACON Deliverable D5.1.2. 334 pp.

[27] Villar, M.V. 2005. MX-80 bentonite. Thermo-hydro-mechanical characterisation performed at CIEMAT in the context of the Prototype Project. Informes Técnicos CIEMAT 1053. CIEMAT, Madrid, 39 pp.

[28] Villar, M.V. 2013. Long-term THM tests reports: Isothermal infiltration tests with materials from the HE-E. PEBS Deliverable 2.2-7.2. CIEMAT Technical Report CIEMAT/DMA/2G210/07/2013. Madrid, 32 pp.

[29] Villar MV, Gómez-Espina R, Gutiérrez-Nebot L, 2012. Basal spacings of compacted bentonite. Applied Clay Science 65-66. Pp. 95-105.

[30] Villar, M.V., Iglesias, R.J., García-Siñeriz, J.L., Lloret, A., Huertas, F. 2020. Physical evolution of a bentonite buffer during 18 years of heating and hydration. Engineering Geology 264. 105408. https://doi.org/10.1016/j.enggeo.2019.105408

[31] Villar, M.V., Iglesias, R.J., Gutiérrez-Álvarez, C., Carbonell, B. 2021. Pellets/block bentonite barriers: Laboratory study of their evolution upon hydration. Engineering Geology 292.106272. https://doi.org/10.1016/j.enggeo.2021.106272

# APPENDIXES

## APPENDIX I: VALUES RECORDED BY SENSORS

*Table A- I. Selected values of relative humidity, temperature and pressure recorded by sensors (sensor "up" placed at 12.8 cm from the bottom porous stone, sensor "mid" at 7.8 cm and sensor "dwn" at 1.3 cm)*

| TIME (days) | RH-up (%) | RH-mid (%) | RH-dwn (%) | *T* (°C) | *P*-up (MPa) | *P*-mid (MPa) | *P*-dwn (MPa) | Pore *P* (MPa) |
|---|---|---|---|---|---|---|---|---|
| 0 | 43 | 42 | 41 | 24 | -0.01 | -0.01 | -0.02 | 0.094 |
| 1 | 43 | 43 | - | 25 | -0.01 | -0.10 | 0.70 | 0.108 |
| 2 | 43 | 44 | 100 | 25 | -0.02 | -0.14 | 0.69 | 0.094 |
| 3 | 43 | 45 | 100 | 25 | -0.02 | -0.15 | 0.70 | 0.094 |
| 4 | 43 | 47 | 100 | 25 | -0.01 | -0.28 | 0.84 | 0.094 |
| 5 | 43 | 48 | 100 | 25 | 0.00 | -0.30 | 0.84 | 0.094 |
| 6 | 43 | 49 | 100 | 25 | -0.03 | -0.27 | 0.93 | 0.094 |
| 7 | 43 | 50 | 100 | 24 | -0.03 | -0.30 | 1.00 | 0.094 |
| 8 | 43 | 51 | 100 | 24 | -0.03 | -0.26 | 1.08 | 0.094 |
| 9 | 43 | 51 | 100 | 24 | -0.03 | -0.38 | 1.22 | 0.094 |
| 13 | 44 | 54 | 100 | 23 | -0.03 | -0.43 | 1.40 | 0.095 |
| 15 | 45 | 56 | 100 | 23 | -0.04 | -0.35 | 1.43 | 0.095 |
| 17 | 45 | 57 | 100 | 24 | -0.02 | -0.47 | 1.49 | 0.094 |
| 19 | 46 | 58 | 100 | 24 | -0.02 | -0.49 | 1.55 | 0.094 |
| 21 | 46 | 60 | 100 | 24 | -0.01 | -0.50 | 1.58 | 0.095 |
| 23 | 47 | 61 | 100 | 24 | -0.01 | -0.48 | 1.64 | 0.095 |
| 26 | 48 | 63 | 100 | 24 | 0.00 | -0.42 | 1.74 | 0.094 |
| 29 | 49 | 65 | 100 | 24 | -0.01 | -0.27 | 1.83 | 0.095 |
| 33 | 50 | 67 | 100 | 24 | -0.03 | 0.15 | 1.93 | 0.094 |
| 36 | 51 | 69 | 100 | 24 | -0.01 | 0.71 | 2.00 | 0.095 |
| 39 | 52 | 71 | 100 | 23 | 0.00 | 1.16 | 2.14 | 0.095 |
| 41 | 52 | 72 | 100 | 23 | 0.00 | 1.51 | 2.18 | 0.094 |
| 45 | 53 | 73 | 100 | 23 | 0.00 | 2.13 | 2.22 | 0.095 |
| 51 | 55 | 76 | 100 | 23 | 0.01 | 2.68 | 2.38 | 0.094 |
| 57 | 57 | 78 | 100 | 23 | 0.02 | 3.10 | 2.48 | 0.095 |
| 63 | 58 | 79 | 100 | 23 | 0.03 | 3.47 | 2.54 | 0.094 |
| 69 | 61 | 81 | 100 | 26 | 0.05 | 3.67 | 2.64 | 0.095 |
| 75 | 62 | 82 | 100 | 23 | 0.05 | 3.97 | 2.68 | 0.094 |
| 81 | 64 | 83 | 100 | 22 | 0.08 | 4.02 | 2.76 | 0.093 |
| 87 | 66 | 84 | 100 | 22 | 0.08 | 4.11 | 2.88 | 0.095 |
| 94 | 68 | 85 | 100 | 24 | 0.13 | 4.18 | 2.87 | 0.094 |
| 100 | 70 | 86 | 100 | 21 | 0.12 | 4.26 | 2.97 | 0.094 |
| 106 | 71 | 87 | 100 | 22 | 0.13 | 4.29 | 3.03 | 0.094 |
| 112 | 73 | 88 | 100 | 21 | 0.15 | 4.30 | 3.10 | 0.095 |
| 118 | 75 | 88 | 100 | 23 | 0.16 | 4.24 | 3.06 | 0.094 |
| 131 | 78 | 90 | 100 | 22 | 0.15 | 4.24 | 3.23 | 0.095 |
| 143 | 81 | 91 | 100 | 21 | 0.13 | 4.20 | 3.30 | 0.097 |
| 156 | 83 | 92 | 100 | 20 | 0.10 | 4.25 | 3.34 | 0.099 |
| 168 | 85 | 92 | 100 | 21 | 0.11 | 4.10 | 3.40 | 0.102 |
| 180 | 86 | 93 | 100 | 24 | 0.08 | 4.04 | 3.38 | 0.105 |
| 192 | 88 | 94 | 100 | 22 | 0.10 | 4.01 | 3.45 | 0.104 |
| 204 | 89 | 94 | 100 | 23 | 0.19 | 3.97 | 3.44 | 0.105 |
| 216 | 90 | 95 | 100 | 22 | 0.32 | 3.92 | 3.50 | 0.104 |
| 228 | 91 | 95 | 100 | 24 | 0.54 | 3.91 | 3.54 | 0.103 |
| 240 | 92 | 95 | 100 | 22 | 0.78 | 3.90 | 3.57 | 0.101 |
| 254 | 92 | 95 | 100 | 23 | 1.04 | 3.98 | 3.54 | 0.102 |
| 263 | 93 | 96 | 100 | 24 | 1.22 | 3.98 | 3.62 | 0.102 |
| 275 | 93 | 96 | 100 | 23 | 1.44 | 3.96 | 3.65 | 0.101 |
| 288 | 94 | 96 | 100 | 22 | 1.61 | 4.09 | 3.75 | 0.100 |
| 300 | 94 | 96 | 100 | 23 | 1.75 | 4.09 | 3.70 | 0.099 |
| 312 | 94 | 97 | 100 | 22 | 1.89 | 4.04 | 3.74 | 0.099 |

*Table A- I. (continuación) Selected values of relative humidity, temperature and pressure recorded by sensors (sensor "up" placed at 12.8 cm from the bottom porous stone, sensor "mid" at 7.8 cm and sensor "dwn" at 1.3 cm).*

| TIME (days) | RH-up (%) | RH-mid (%) | RH-dwn (%) | *T* (°C) | *P*-up (MPa) | *P*-mid (MPa) | *P*-dwn (MPa) | Pore *P* (MPa) |
|---|---|---|---|---|---|---|---|---|
| 324 | 95 | 97 | 100 | 23 | 1,99 | 4,17 | 3,81 | 0,099 |
| 337 | 95 | 97 | 100 | 23 | 2,12 | 4,15 | 3,80 | 0,098 |
| 351 | 95 | 97 | 100 | 23 | 2,22 | 4,23 | 3,84 | 0,097 |
| 363 | 96 | 97 | 100 | 24 | 2,34 | 4,26 | 3,89 | 0,096 |
| 375 | 96 | 97 | 100 | 23 | 2,42 | 4,33 | 3,89 | 0,094 |
| 387 | 96 | 97 | 100 | 23 | 2,53 | 4,32 | 3,95 | 0,093 |
| 399 | 96 | 98 | 100 | 22 | 2,64 | 4,33 | 3,99 | 0,093 |
| 411 | 96 | 98 | 100 | 23 | 2,72 | 4,35 | 3,98 | 0,094 |
| 423 | 97 | 98 | 100 | 21 | 2,81 | 4,41 | 4,10 | 0,093 |
| 435 | 96 | 98 | 100 | 25 | 2,91 | 4,47 | 4,04 | 0,097 |
| 448 | 97 | 98 | 100 | 23 | 3,00 | 4,51 | 4,13 | 0,094 |
| 460 | 97 | 98 | 100 | 24 | 3,12 | 4,57 | 4,07 | 0,094 |
| 473 | 97 | 98 | 100 | 23 | 3,25 | 4,66 | 4,14 | 0,092 |
| 485 | 97 | 98 | 100 | 21 | 3,34 | 4,81 | 4,19 | 0,091 |
| 497 | 98 | 99 | 100 | 20 | 3,47 | 4,77 | 4,19 | 0,091 |
| 509 | 98 | 99 | 100 | 21 | 3,56 | 4,91 | 4,20 | 0,094 |
| 522 | 98 | 99 | 100 | 19 | 3,68 | 4,96 | 4,25 | 0,096 |
| 534 | 99 | 100 | 100 | 16 | 3,82 | 5,11 | 4,41 | 0,098 |
| 546 | 98 | 99 | 100 | 22 | 3,90 | 5,08 | 4,28 | 0,110 |
| 558 | 99 | 99 | 100 | 19 | 4,04 | 5,14 | 4,28 | 0,114 |
| 570 | 98 | 99 | 100 | 21 | 4,29 | 5,46 | 4,45 | 0,122 |
| 582 | 98 | 99 | 100 | 22 | 4,45 | 5,60 | 4,47 | 0,130 |
| 596 | 99 | 99 | 100 | 21 | 4,61 | 5,85 | 4,50 | 0,137 |
| 611 | 99 | 99 | 100 | 23 | 4,95 | 6,19 | 4,57 | 0,146 |
| 623 | 99 | 99 | 100 | 21 | 4,95 | 6,13 | 4,54 | 0,149 |
| 635 | 99 | 99 | 100 | 20 | 5,07 | 6,12 | 4,48 | 0,153 |
| 647 | 99 | 99 | 100 | 20 | 5,13 | 6,15 | 4,58 | 0,157 |
| 659 | 99 | 99 | 100 | 21 | 5,48 | 6,50 | 4,67 | 0,161 |
| 671 | 99 | 99 | 100 | 21 | 5,53 | 6,43 | 4,65 | 0,163 |
| 683 | 99 | 99 | 100 | 20 | 5,37 | 6,26 | 4,54 | 0,163 |
| 695 | 99 | 99 | 100 | 23 | 5,76 | 6,66 | 4,75 | 0,170 |
| 707 | 99 | 99 | 100 | 22 | 5,47 | 6,24 | 4,48 | 0,173 |
| 719 | 99 | 99 | 100 | 23 | 5,61 | 6,54 | 4,61 | 0,176 |
| 732 | 99 | 99 | 100 | 22 | 5,55 | 6,34 | 4,54 | 0,175 |
| 744 | 99 | 99 | 100 | 23 | 5,60 | 6,38 | 4,63 | 0,179 |
| 756 | 98 | 99 | 100 | 23 | 5,59 | 6,38 | 4,64 | 0,181 |
| 768 | 98 | 99 | 100 | 23 | 5,64 | 6,43 | 4,62 | 0,179 |
| 780 | 98 | 99 | 100 | 22 | 5,63 | 6,48 | 4,66 | 0,177 |
| 793 | 99 | 99 | 100 | 22 | 5,65 | 6,55 | 4,67 | 0,176 |
| 805 | 99 | 99 | 100 | 21 | 5,64 | 6,45 | 4,64 | 0,176 |
| 817 | 99 | 99 | 100 | 20 | 5,60 | 6,40 | 4,67 | 0,173 |
| 829 | 99 | 99 | 100 | 21 | 5,66 | 6,41 | 4,72 | 0,175 |
| 841 | 98 | 99 | 100 | 21 | 5,73 | 6,47 | 4,69 | 0,177 |
| 853 | 99 | 100 | - | 20 | 5,81 | 6,59 | 4,82 | 0,175 |
| 865 | 99 | 100 | - | 21 | 5,74 | 6,42 | 4,66 | 0,182 |
| 887 | - | 100 | - | - | 5,77 | 6,52 | 4,67 | 0,181 |
| 902 | - | - | 100 | - | 5,82 | 6,49 | 4,73 | 0,173 |
| 914 | - | - | 100 | - | 5,82 | 6,55 | 4,67 | 0,180 |

# APPENDIX II. SUBSAMPLING OF SECTIONS

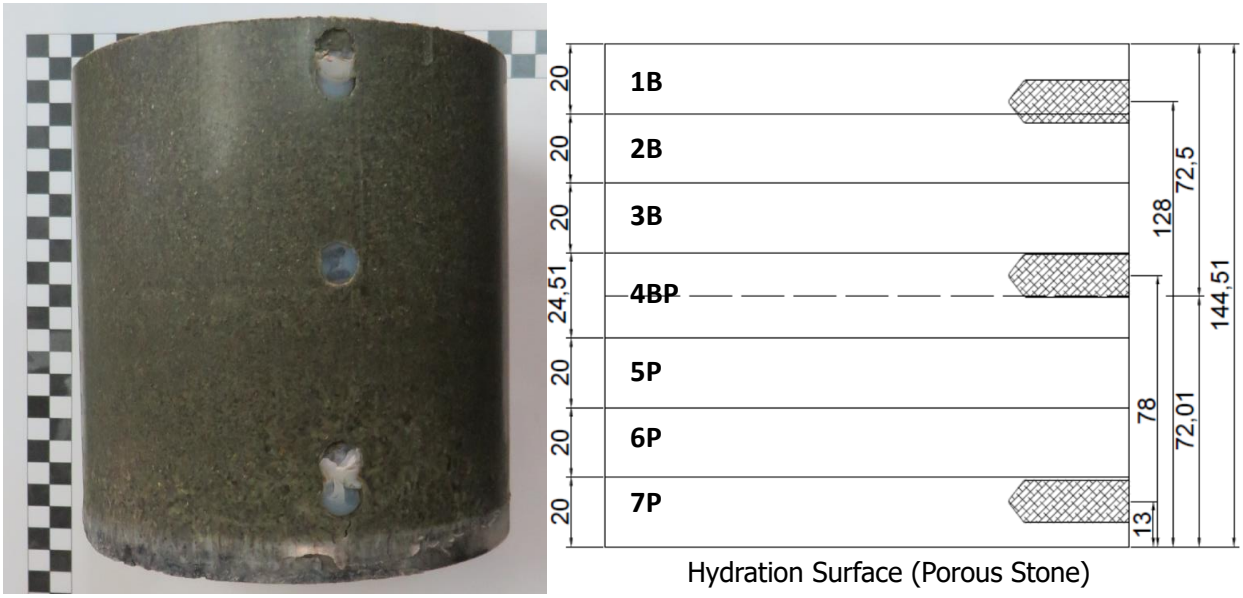


*Figure A- 1. State of the sample on dismantling (left) and sampling scheme of the seven sections (right). The white Teflon® plugs (left) were placed where the RH/T sensors were located (B: Block, P: Pellets, dimensions in millimetres).*

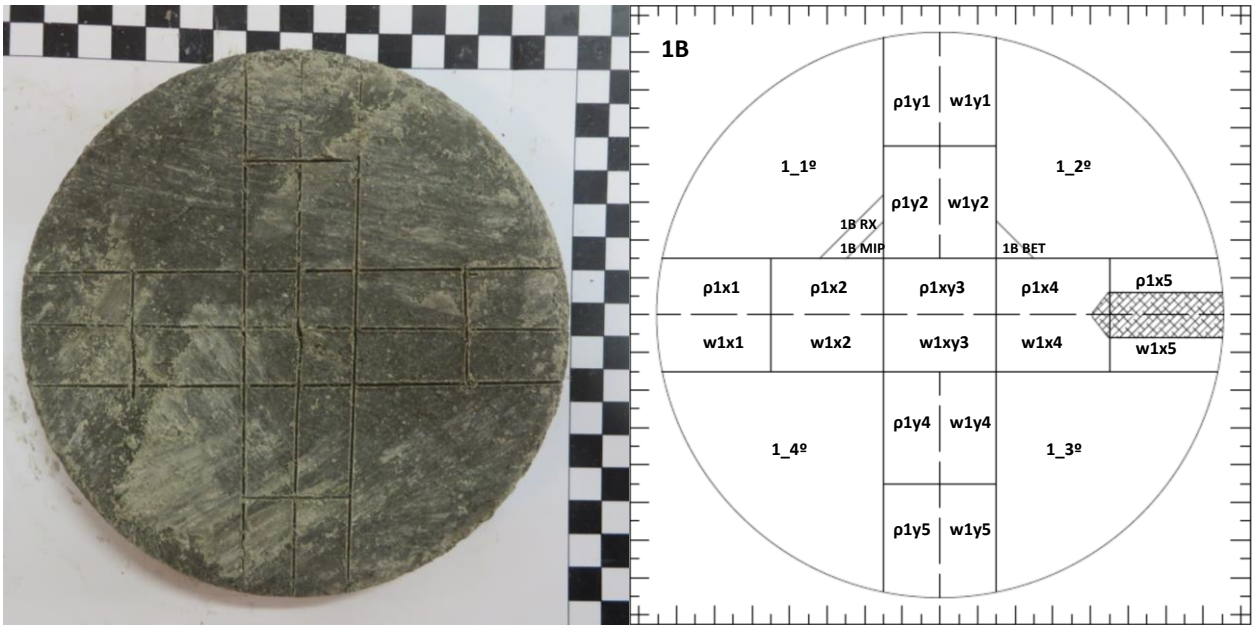


*Figure A- 2. Example of a section before subsampling (left) and subsampling scheme in section 1B (right). The X axis is that of the sensors (samples x1 to x5) and the Y axis is perpendicular to it (samples y1 to y5). The kind of determination for each subsample is: w: water content, ρ: dry density, MIP: mercury intrusion porosimetry, BET:BET specific surface area, RX:X-ray diffraction*

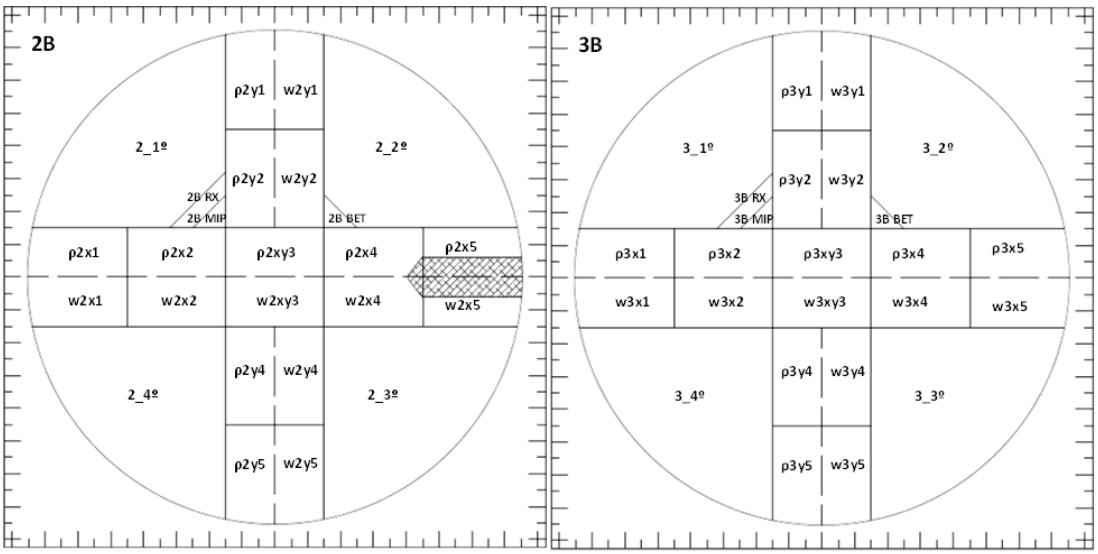


*Figure A- 3. Subsampling scheme in sections 2B and 3B*

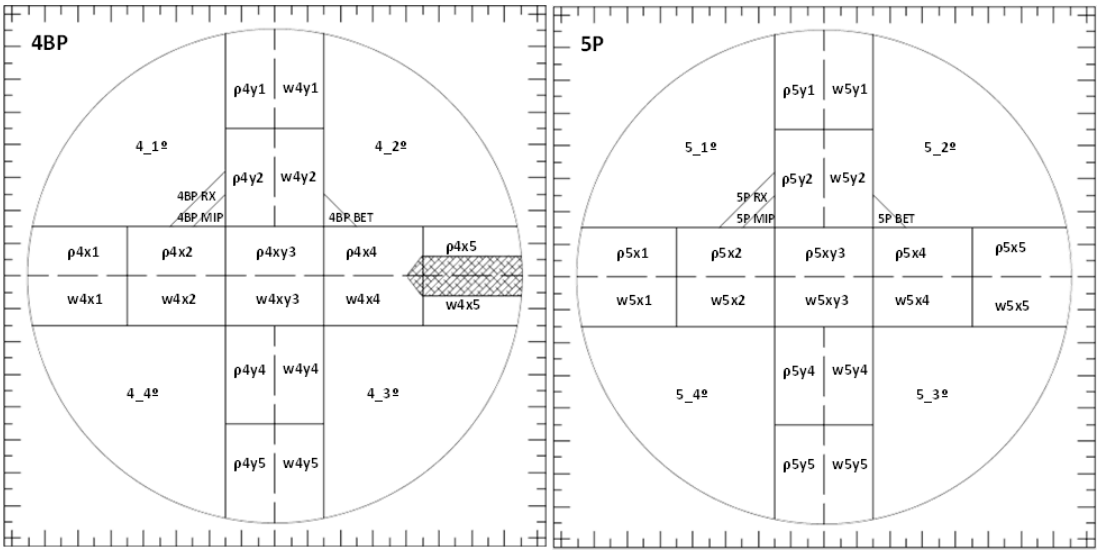


*Figure A- 4. Subsampling scheme in sections 4BP and 5P*

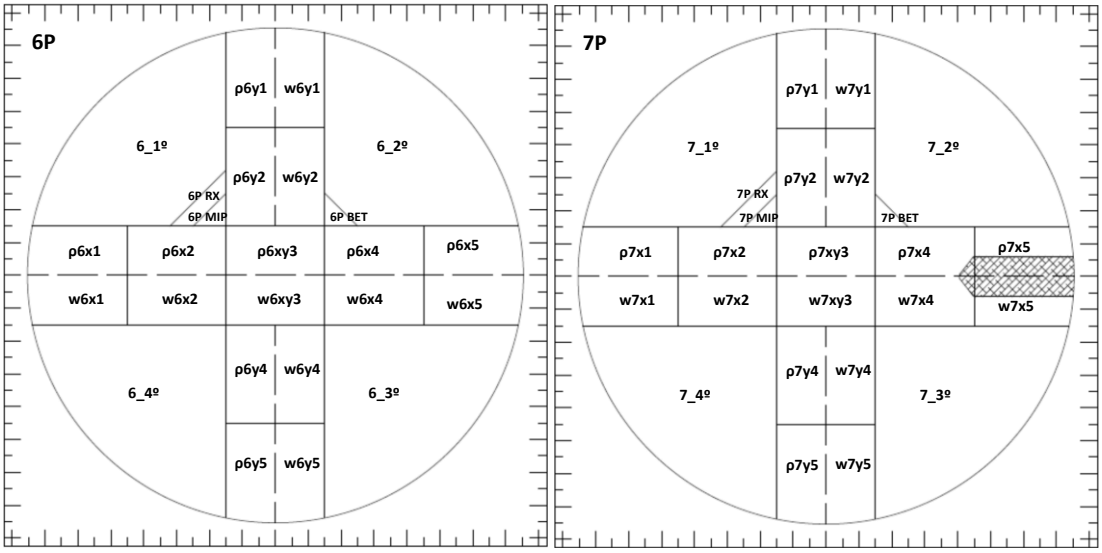


*Figure A- 5. Subsampling scheme in sections 6P and 7P*

## APPENDIX III. FINAL VALUES

Table A- II. Final water content (w), dry density ($\rho_d$) and degree of saturation ($S_r$) of the subsamples analysed

| REFERENCE | SECTION | Distance to bottom (cm) | Distance to axis (cm) | $w$ (%) | $\rho_d$ (g/cm$^3$) | $S_r$ (%) |
|---|---|---|---|---|---|---|
| 7X1 | 7P | 1.00 | 6.10 | 32.9 | 1.42 | 96 |
| 7X5 | 7P | 1.00 | 6.10 | 36.6 | 1.37 | 100 |
| 7Y1 | 7P | 1.00 | 6.10 | 34.0 | 1.41 | 99 |
| 7Y5 | 7P | 1.00 | 6.10 | 33.6 | 1.42 | 98 |
| 7X2 | 7P | 1.00 | 3.35 | 32.5 | 1.45 | 100 |
| 7X4 | 7P | 1.00 | 3.35 | 32.7 | 1.44 | 99 |
| 7Y2 | 7P | 1.00 | 3.35 | 33.0 | 1.45 | 101 |
| 7Y4 | 7P | 1.00 | 3.35 | 32.8 | 1.44 | 98 |
| 7XY3 | 7P | 1.00 | 0.00 | 32.4 | 1.45 | 98 |
| 6X1 | 6P | 3.00 | 6.10 | 29.5 | 1.51 | 98 |
| 6X5 | 6P | 3.00 | 6.10 | 31.6 | 1.45 | 97 |
| 6Y1 | 6P | 3.00 | 6.10 | 30.4 | 1.50 | 99 |
| 6Y5 | 6P | 3.00 | 6.10 | 29.8 | 1.50 | 98 |
| 6X2 | 6P | 3.00 | 3.35 | 30.0 | 1.49 | 97 |
| 6X4 | 6P | 3.00 | 3.35 | 30.6 | 1.48 | 97 |
| 6Y2 | 6P | 3.00 | 3.35 | 30.4 | 1.49 | 99 |
| 6Y4 | 6P | 3.00 | 3.35 | 30.2 | 1.50 | 99 |
| 6XY3 | 6P | 3.00 | 0.00 | 30.3 | 1.48 | 96 |
| 5X1 | 5P | 5.00 | 6.10 | 28.8 | 1.52 | 97 |
| 5X5 | 5P | 5.00 | 6.10 | 29.6 | 1.51 | 98 |
| 5Y1 | 5P | 5.00 | 6.10 | 29.1 | 1.52 | 99 |
| 5Y5 | 5P | 5.00 | 6.10 | 29.0 | 1.52 | 98 |
| 5X2 | 5P | 5.00 | 3.35 | 29.1 | 1.51 | 97 |
| 5X4 | 5P | 5.00 | 3.35 | 29.4 | 1.51 | 98 |
| 5Y2 | 5P | 5.00 | 3.35 | 29.3 | 1.50 | 97 |
| 5Y4 | 5P | 5.00 | 3.35 | 29.4 | 1.50 | 97 |
| 5XY3 | 5P | 5.00 | 0.00 | 29.1 | 1.51 | 97 |
| 4X1 | 4BP | 7.23 | 6.10 | 28.7 | 1.52 | 97 |
| 4X5 | 4BP | 7.23 | 6.10 | 29.0 | 1.51 | 96 |
| 4Y1 | 4BP | 7.23 | 6.10 | 29.2 | 1.52 | 98 |
| 4Y5 | 4BP | 7.23 | 6.10 | 28.9 | 1.53 | 98 |
| 4X2 | 4BP | 7.23 | 3.35 | 29.2 | 1.51 | 96 |
| 4X4 | 4BP | 7.23 | 3.35 | 29.5 | 1.50 | 97 |
| 4Y2 | 4BP | 7.23 | 3.35 | 29.3 | 1.51 | 97 |
| 4Y4 | 4BP | 7.23 | 3.35 | 29.2 | 1.51 | 97 |
| 4XY3 | 4BP | 7.23 | 0.00 | 29.2 | 1.51 | 97 |
| 3X1 | 3B | 9.45 | 6.10 | 29.5 | 1.49 | 95 |
| 3X5 | 3B | 9.45 | 6.10 | 29.2 | 1.49 | 94 |
| 3Y1 | 3B | 9.45 | 6.10 | 29.4 | 1.50 | 96 |
| 3Y5 | 3B | 9.45 | 6.10 | 29.2 | 1.51 | 96 |
| 3X2 | 3B | 9.45 | 3.35 | 29.6 | 1.51 | 98 |
| 3X4 | 3B | 9.45 | 3.35 | 29.6 | 1.50 | 96 |
| 3Y2 | 3B | 9.45 | 3.35 | 29.5 | 1.50 | 96 |
| 3Y4 | 3B | 9.45 | 3.35 | 29.3 | 1.50 | 96 |
| 3XY3 | 3B | 9.45 | 0.00 | 29.6 | 1.50 | 97 |
| 2X1 | 2B | 11.45 | 6.10 | 29.3 | 1.51 | 96 |
| 2X5 | 2B | 11.45 | 6.10 | 29.6 | 1.49 | 95 |
| 2Y1 | 2B | 11.45 | 6.10 | 29.4 | 1.50 | 96 |
| 2Y5 | 2B | 11.45 | 6.10 | 29.4 | 1.50 | 95 |
| 2X2 | 2B | 11.45 | 3.35 | 29.2 | 1.51 | 96 |
| 2X4 | 2B | 11.45 | 3.35 | 29.3 | 1.50 | 95 |
| 2Y2 | 2B | 11.45 | 3.35 | 29.3 | 1.51 | 96 |

Table A- IIIII (continuación). Final water content (w), dry density ($\rho_d$) and degree of saturation ($S_r$) of the subsamples analysed

| REFERENCE | SECTION | Distance to bottom (cm) | Distance to axis (cm) | *w* (%) | $\rho_d$ (g/cm$^3$) | $S_r$ (%) |
|---|---|---|---|---|---|---|
| 2Y4 | 2B | 11.45 | 3.35 | 29.5 | 1.50 | 97 |
| 2XY3 | 2B | 11.45 | 0.00 | 29.1 | 1.50 | 95 |
| 1X1 | 1B | 13.45 | 6.10 | 29.5 | 1.50 | 96 |
| 1X5 | 1B | 13.45 | 6.10 | 30.4 | 1.46 | 94 |
| 1Y1 | 1B | 13.45 | 6.10 | 29.8 | 1.49 | 96 |
| 1Y5 | 1B | 13.45 | 6.10 | 30.1 | 1.48 | 95 |
| 1X2 | 1B | 13.45 | 3.35 | 28.8 | 1.51 | 95 |
| 1X4 | 1B | 13.45 | 3.35 | 29.4 | 1.51 | 97 |
| 1Y2 | 1B | 13.45 | 3.35 | 29.5 | 1.50 | 96 |
| 1Y4 | 1B | 13.45 | 3.35 | 29.1 | 1.50 | 96 |
| 1XY3 | 1B | 13.45 | 0.00 | 28.8 | 1.51 | 95 |

## APPENDIX IV. CONTOUR PLOTS

### *2D CONTOUR REPRESENTATIONS OF THE X VERTICAL SECTION*

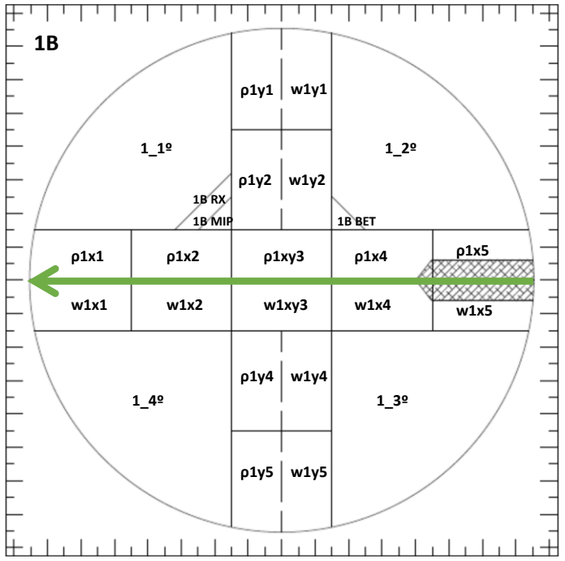


*Figure A- 6. The green arrow indicates the position of the vertical cross-section obtained through the X-diameter of the column*

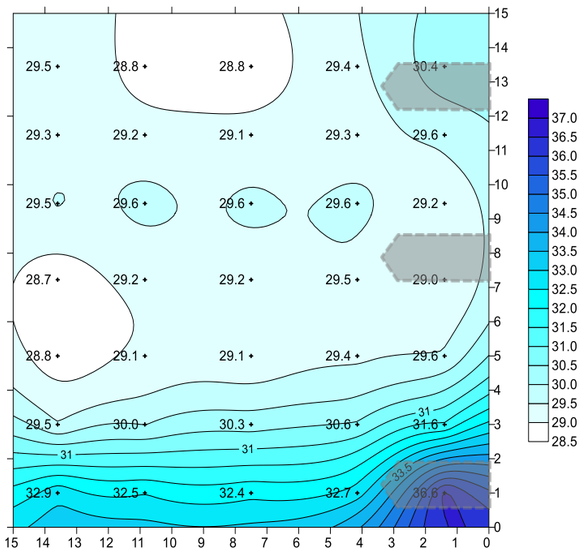


*Figure A- 7. 2D contour representation of water content ( %) of the vertical section along the X diameter (see Figure A- 6 for location). The shadowed areas indicate the position of the RH/T sensors*

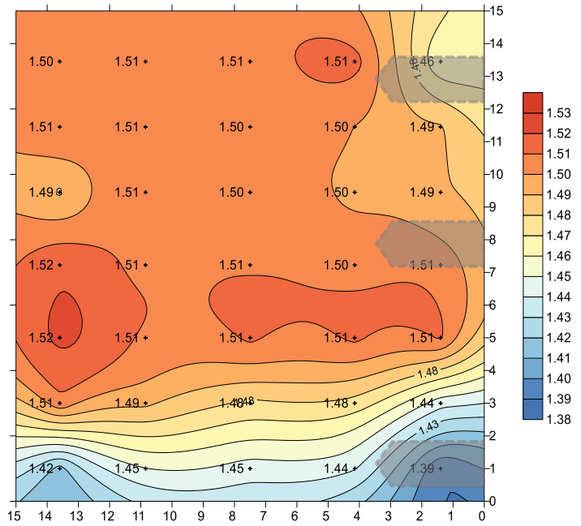


*Figure A- 8. 2D contour representation of dry density ( g/cm$^3$) of the vertical section along the X diameter. The shadowed areas indicate the position of the RH/T sensors*

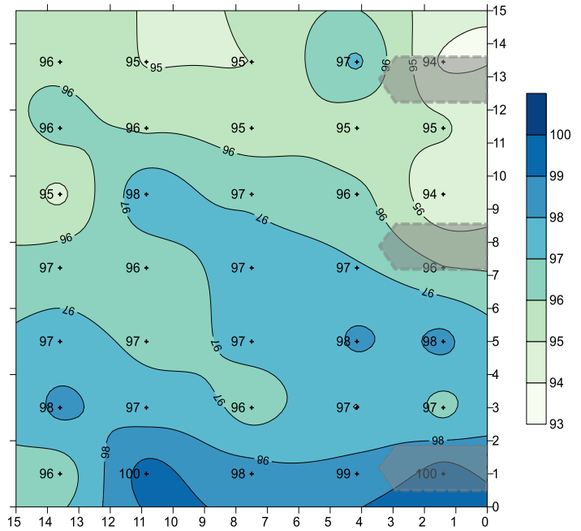


*Figure A- 9. 2D contour representation of degree of saturation ( %) of the vertical section along the X diameter. The shadowed areas indicate the position of the RH/T sensors*

## 2D CONTOUR REPRESENTATIONS OF THE Y VERTICAL SECTION

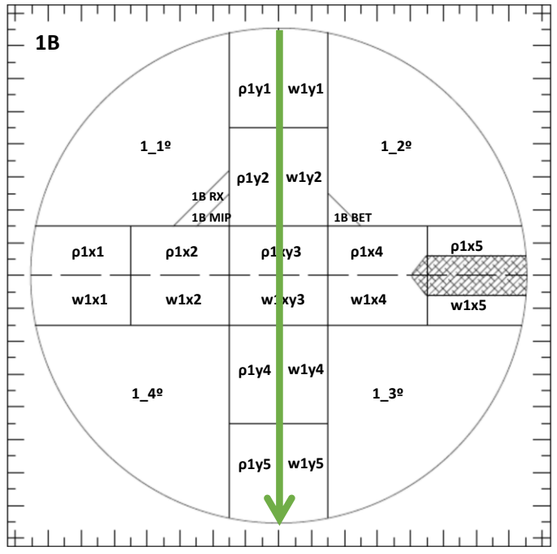


*Figure A- 10. The green arrow indicates the position of the vertical cross-section obtained through the Y-diameter of the column*

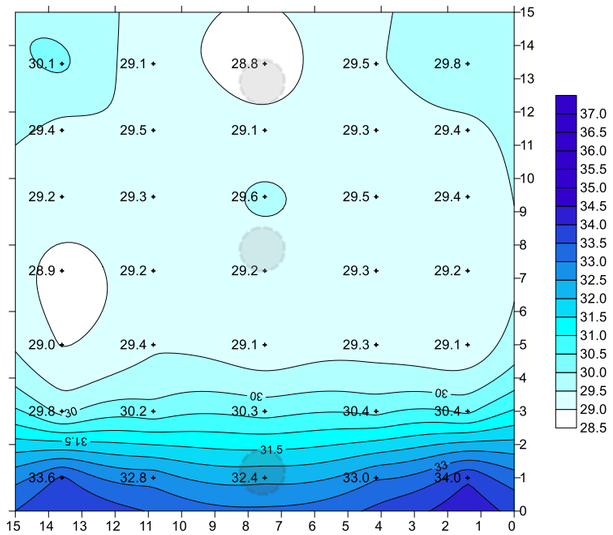


*Figure A- 11. 2D contour representation of water content ( %) of the vertical section along the Y diameter (see Figure A- 10 for location). The shadowed areas indicate the position of the RH/T sensors*

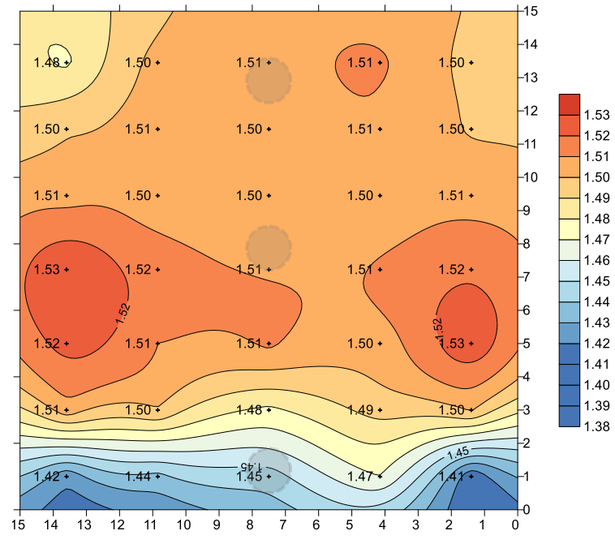


*Figure A- 12. 2D contour representation of dry density (g/cm³) of the vertical section along the Y diameter. The shadowed areas indicate the position of the RH/T sensors*

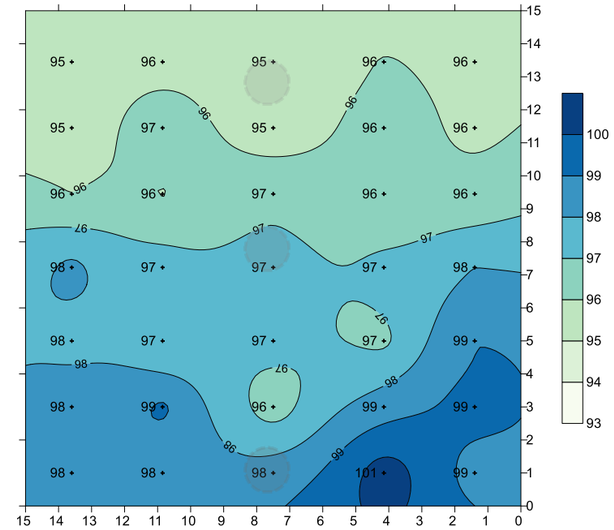


*Figure A- 13. 2D contour representation of degree of saturation ( %) of the vertical section along the Y diameter. The shadowed areas indicate the position of the RH/T sensors*

## 2D CONTOUR REPRESENTATIONS OF LATERAL DEVELOPMENTS OF THE COLUMN

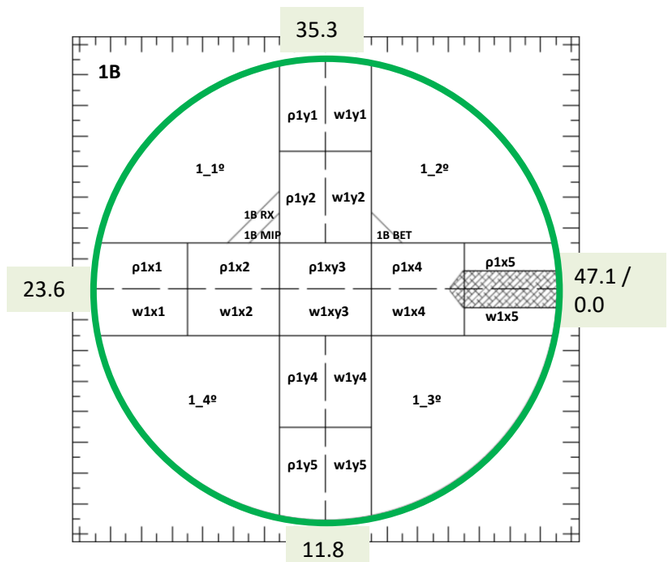


*Figure A- 14. The green circle is a cross-section of the surface developed (lateral external surface)*

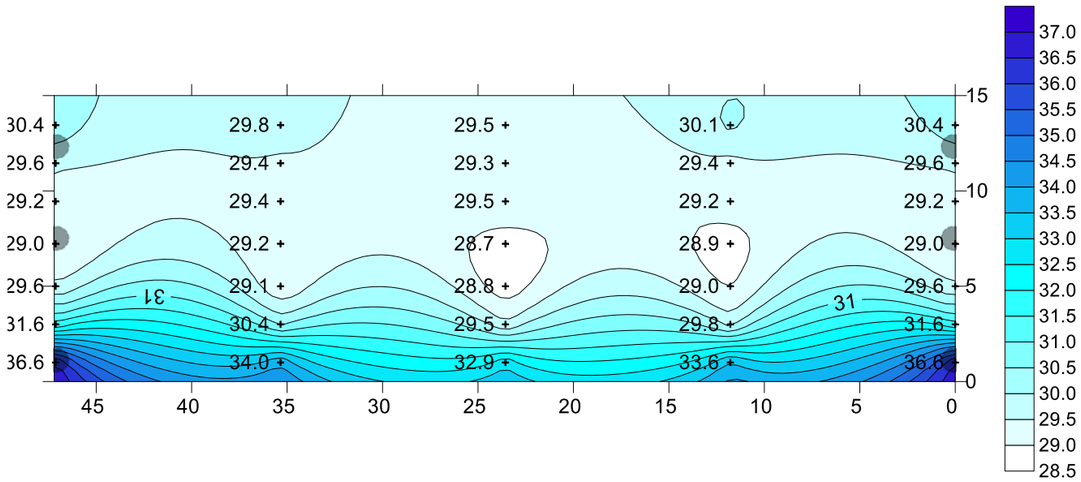


*Figure A- 15. 2D contour representation of water content ( %) corresponding to the development of the lateral surface of the column. The position of the RH/T sensors is indicated with shadowed semicircles*

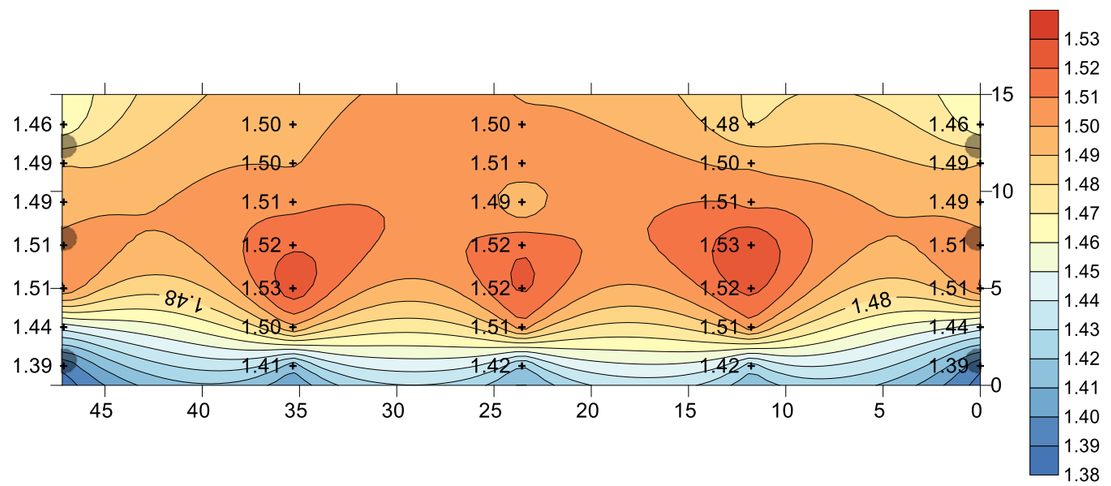


*Figure A- 16. 2D contour representation of dry density (g/cm³) corresponding to the development of the lateral surface of the column. The position of the RH/T sensors is indicated with shadowed semicircles*

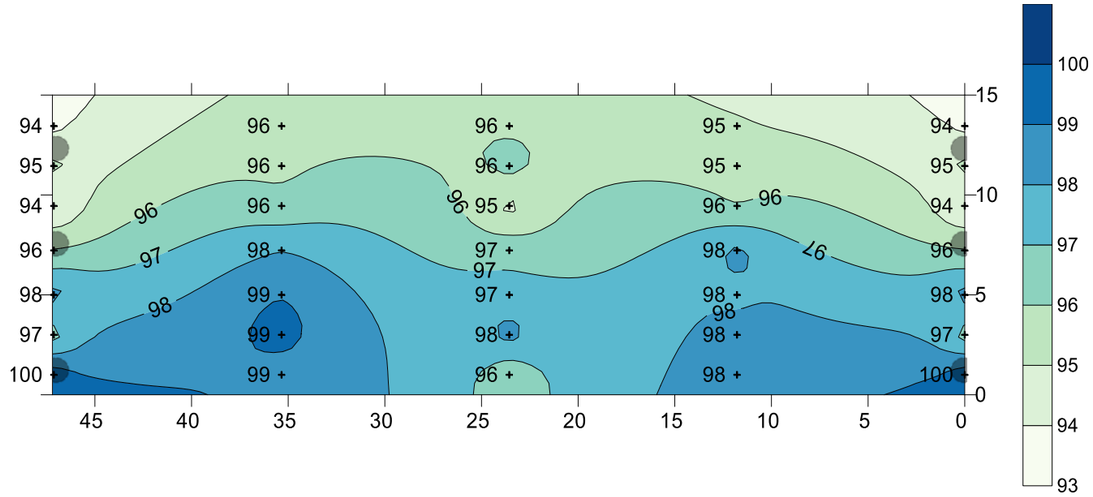


*Figure A- 17. 2D contour representation of saturation degree ( %) corresponding to the development of the lateral surface of the column. The position of the RH/T sensors is indicated with shadowed semicircles*

## 2D CONTOUR REPRESENTATIONS OF THE INTERMEDIATE DEVELOPMENTS OF THE COLUMN

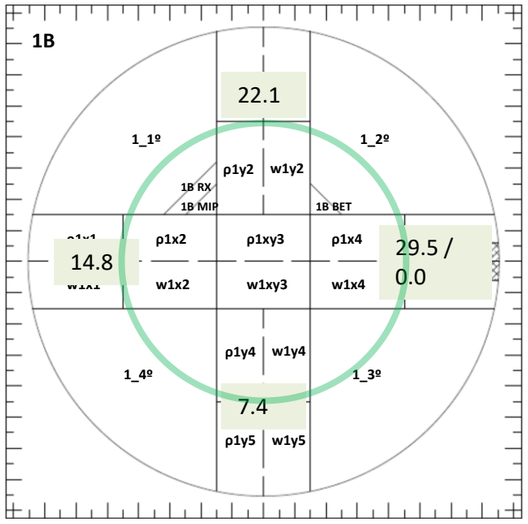


*Figure A- 18. The green circle is a cross-section of the surface developed (lateral surface at 4.7 cm from the axis)*

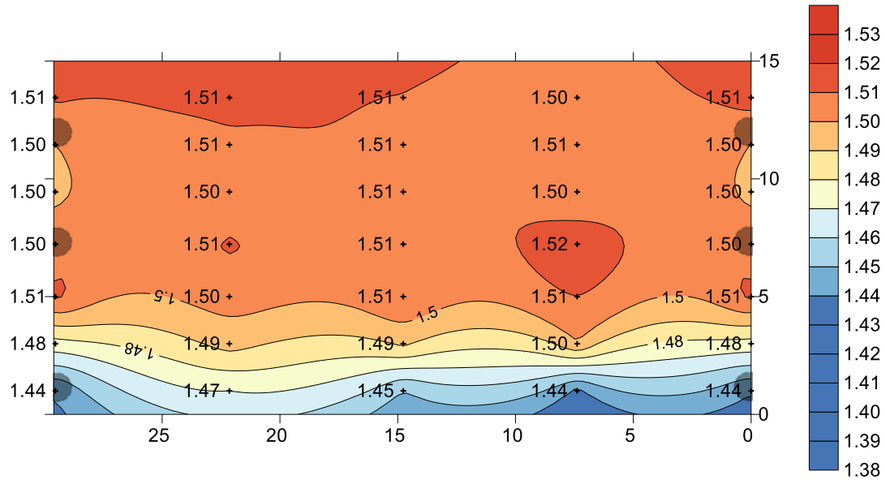


*Figure A- 20. 2D contour representation of dry density (g/cm$^3$) corresponding to the development of the column at 4.7 cm from the axis. The position of the RH/T sensors is indicated with shadowed semicircles*

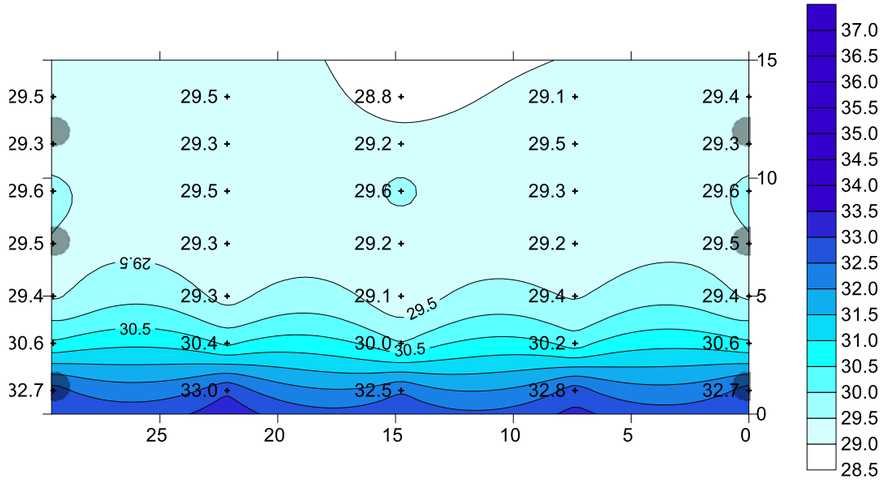


*Figure A- 19. 2D contour representation of water content ( %) corresponding to the development of the column at 4.7 cm from the axis. The position of the RH/T sensors is indicated with shadowed semicircles*

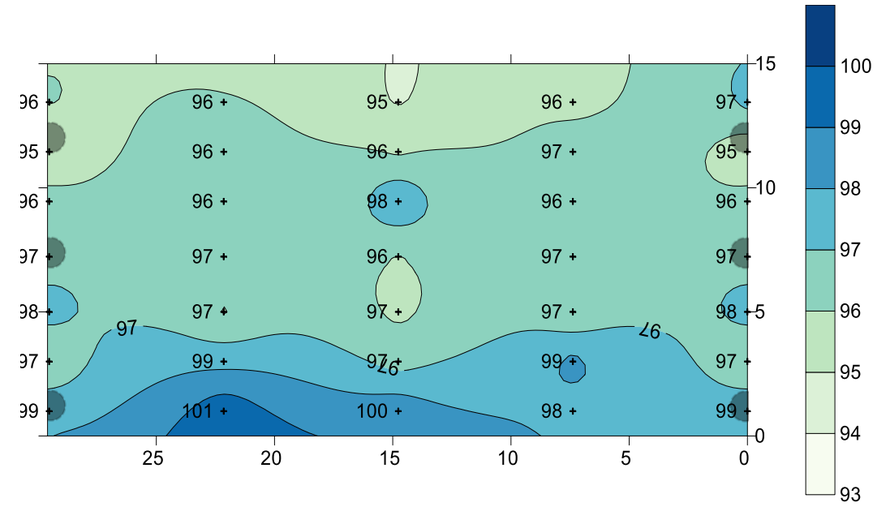


*Figure A- 21. 2D contour representation of the degree of saturation ( %) corresponding to the development of the column at 4.7 cm from the axis. The position of the RH/T sensors is indicated with shadowed semicircles*

## 2D CONTOUR REPRESENTATIONS OF HORIZONTAL SECTIONS

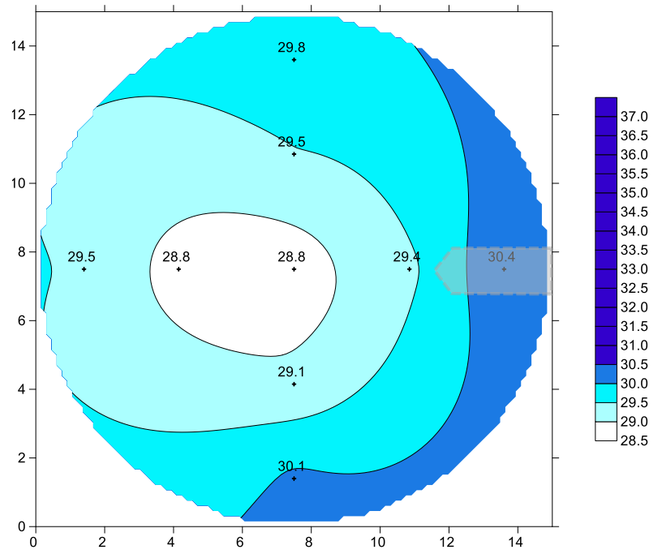


*Figure A- 22. 2D contour representation of water content ( %) of horizontal section 1B (see Appendix 2 for location)*

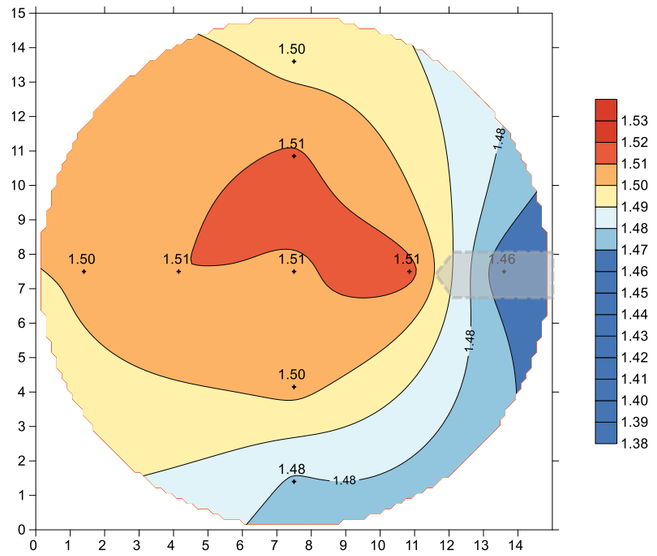


*Figure A- 23. 2D contour representation of dry density (g/cm$^3$) of horizontal section 1B (see Appendix 2 for location)*

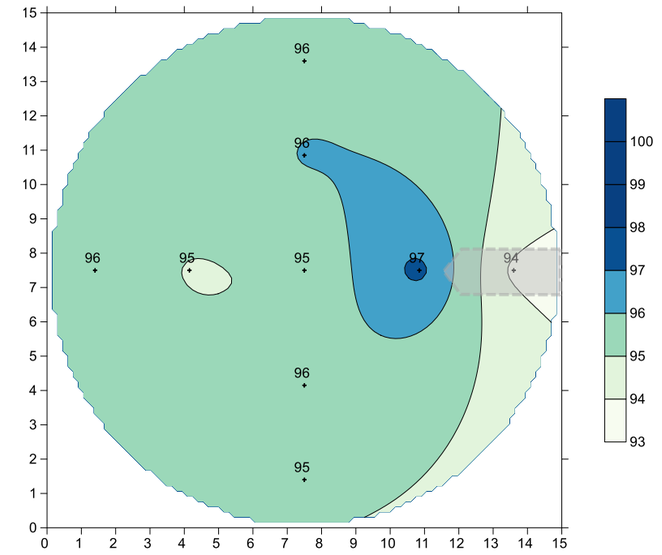


*Figure A- 24. 2D contour representation of degree of saturation ( %) of horizontal section 1B (see Appendix 2 for location)*

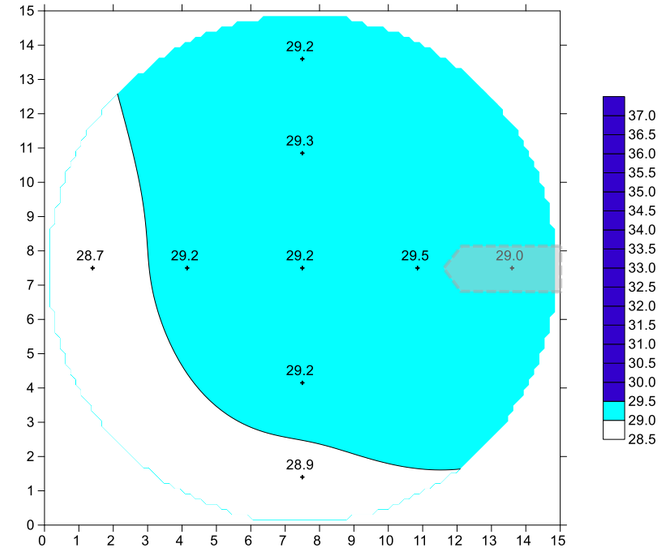


*Figure A- 25. 2D contour representation of water content ( %) of horizontal section 4BP (see Appendix 2 for location)*

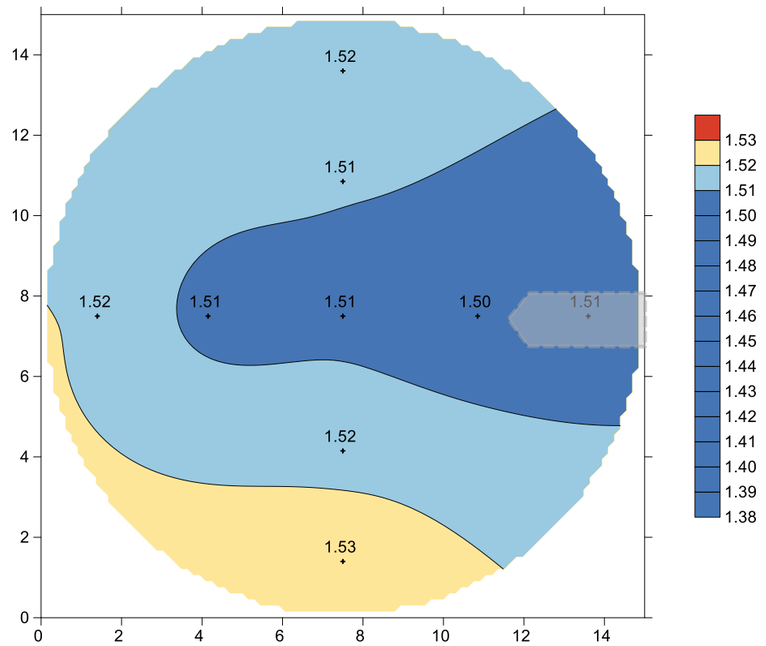


*Figure A- 26. 2D contour representation of dry density (g/cm$^3$) of horizontal section 4BP (see Appendix 2 for location)*

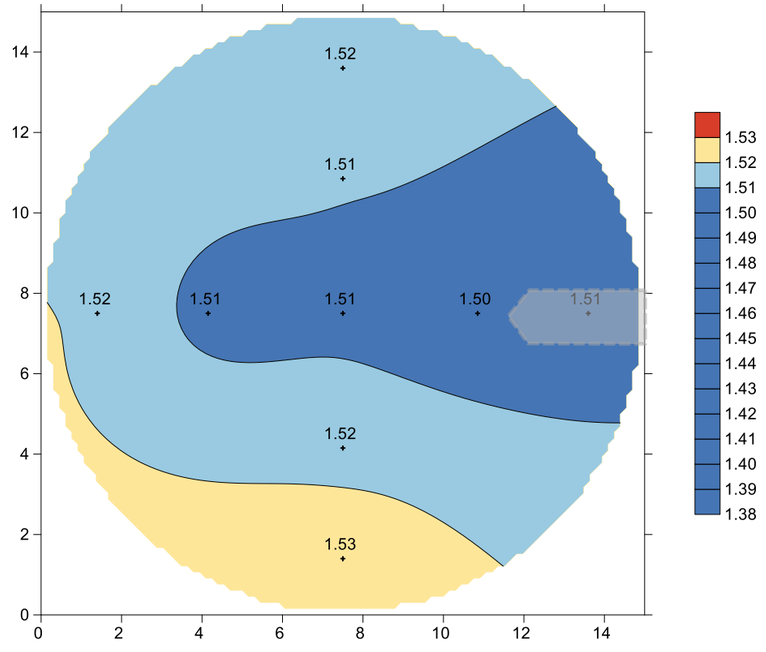


*Figure A- 27. 2D contour representation of degree of saturation ( %) of horizontal section 4BP (see Appendix 2 for location)*

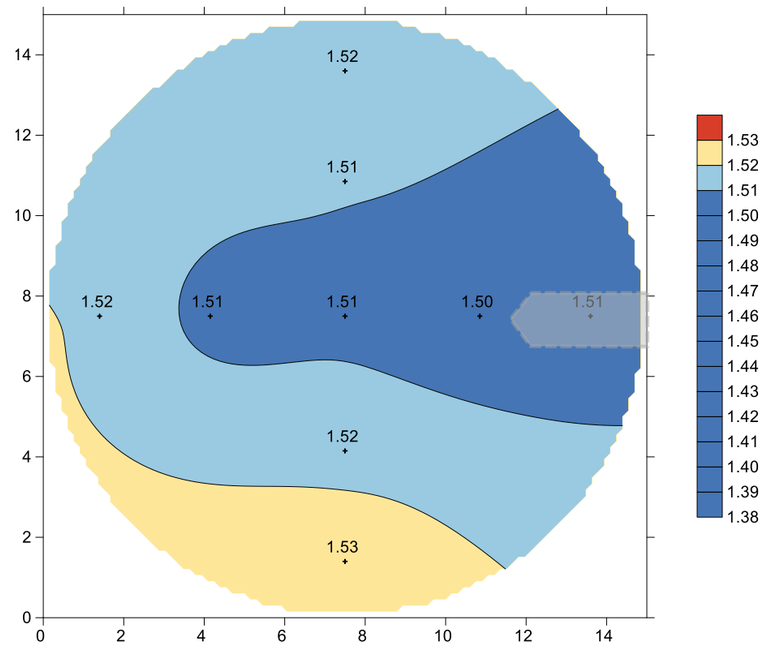


*Figure A- 28. 2D contour representation of water content ( %) of horizontal section 7P (see Appendix 2 for location)*

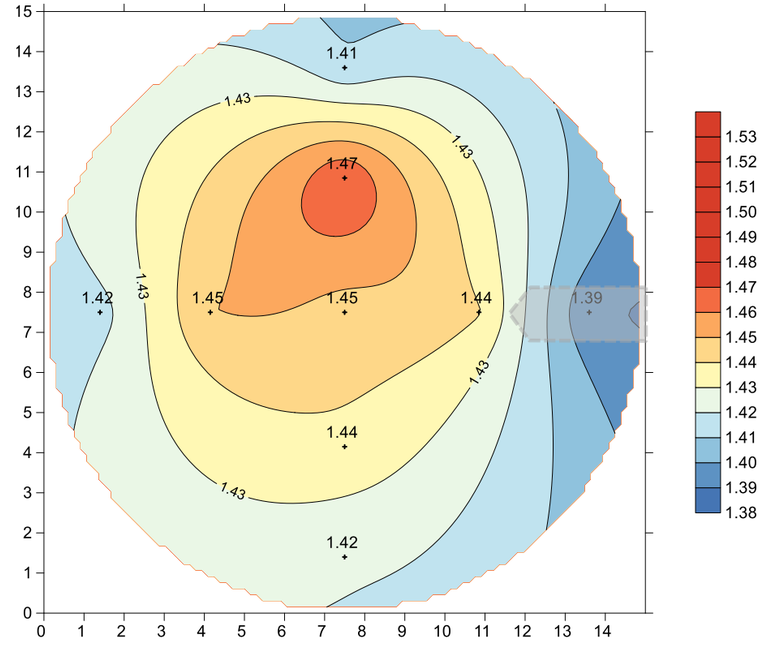


*Figure A- 29. 2D contour representation of dry density (g/cm3) of horizontal section 7P (see Appendix 2 for location)*

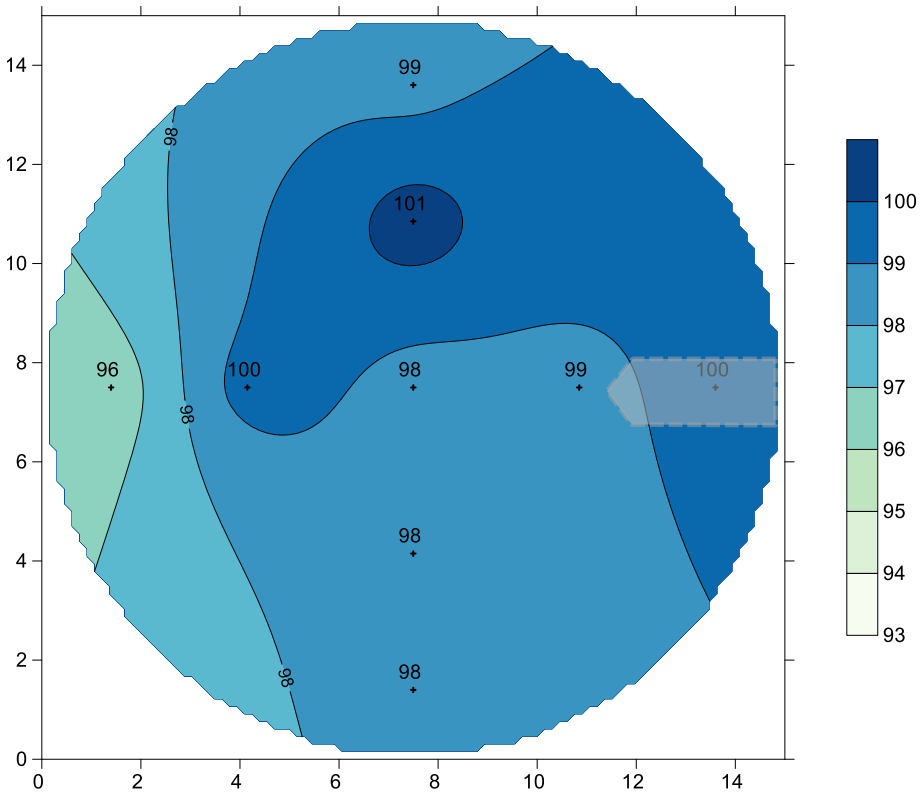


*Figure A- 30. 2D contour representation of degree of saturation ( %) of horizontal section 7P (see Appendix 2 for location)*


2695-8864